JCI The Journal of Clinical Investigation

Transcriptomic profiling after B-cell depletion reveals central and peripheral immune cell changes in multiple sclerosis

Jessica Wei, … , Pierre-Paul Axisa, David A. Hafler

J Clin Invest. 2025. https://doi.org/10.1172/JCI182790.

Research In-Press Preview **Autoimmunity** **Immunology**

Multiple sclerosis (MS) is a complex genetically mediated autoimmune disease of the central nervous system where anti-CD20-mediated B cell depletion is remarkably effective in the treatment of early disease. While previous studies investigated the effect of B cell depletion on select immune cell subsets using flow cytometry-based methods, the therapeutic impact on patient immune landscape is unknown. In this study, we explored how B cell depleting therapies modulate the immune landscape using single-cell RNA sequencing (scRNAseq). We demonstrate that B cell depletion leads to cell type-specific changes in the abundance and function of CSF macrophages and peripheral blood monocytes. Specifically, a CSF-specific macrophage population with an anti-inflammatory transcriptomic signature and peripheral $CD16^+$ monocytes increased in frequency post-B cell depletion. This was accompanied by increases in TNFα messenger RNA and protein in monocytes post-B cell depletion, consistent with the finding that anti-TNFα treatment exacerbates autoimmune activity in MS. In parallel, B cell depletion induced changes in peripheral $CD4^+$ T cell populations, including increases in the frequency of $TIGIT^+$ regulatory T cells and marked decreases in the frequency of myelin peptide loaded-tetramer binding $CD4^+$ T cells. Collectively, this study provides an exhaustive transcriptomic map of immunological changes, revealing different cell-type specific reprogramming as a result of B cell depletion treatment in MS.

Transcriptomic profiling after B-cell depletion reveals central and peripheral immune cell changes in multiple sclerosis

Jessica Wei[1,2*†], Jeonghyeon Moon[1,2*], Yoshiaki Yasumizu[1,2,3], Le Zhang[1], Khadir Radassi[1], Nicholas Buitrago-Pocasangre[1], M. Elizabeth Deerhake[1], Nicolas Strauli[4], Chun-Wei Chen[4‡], Ann Herman[4], Rosetta Pedotti[5], Catarina Raposo[5], Isaiah Yim[6], Jenna Pappalardo[1,2¶], Erin E. Longbrake[1], Tomokazu S. Sumida[1], Pierre-Paul Axisa[1,2,7#§], David A. Hafler[1,2,8#§]

Affiliations

1. Department of Neurology, Yale School of Medicine, New Haven, CT, USA
2. Department of Immunobiology, Yale School of Medicine, New Haven, CT, USA
3. Department of Experimental Immunology, Immunology Frontier Research Center, Osaka University, Suita, Osaka, Japan
4. Genentech, San Francisco, CA
5. Roche, Basel, Switzerland
6. Department of Biomedical Engineering, Yale University, New Haven, CT, USA
7. Centre de recherches en cancérologie de Toulouse (CRCT), Inserm, Toulouse, France
8. Broad Institute, Boston, MA, USA

* equal contribution

# equal contribution

† present address: Nkarta Inc., San Franscisco, CA, USA

‡ present address: Therapeutic Discovery Division, University of Texas MD Anderson Cancer Center, Houston, TX, USA

¶ present address: Arcus Biosciences, Hayward, CA, USA

§ correspondence: Pierre-Paul Axisa, Centre de recherches en cancérologie de Toulouse (CRCT), Inserm, 2 avenue Hubert Curien, 31100 Toulouse, France. Phone : +33.5.82.74.17.62. Email : pierre-paul.axisa@inserm.fr. David A. Hafler, Departments of Neurology and Immunobiology, Yale School of Medicine, 300 George Street, 3rd floor, New Haven, Connecticut 06511, USA. Phone: 203.737.4802; Email: david.hafler@yale.edu.

Declaration of Interests

D.A.H. has received research funding from Bristol-Myers Squibb, Novartis, Sanofi, and Genentech. He has been a consultant for Bayer Pharmaceuticals, Repertoire Inc, Bristol Myers Squibb, Compass Therapeutics, EMD Serono, Genentech, Juno therapeutics, Novartis Pharmaceuticals, Proclara Biosciences, Sage Therapeutics, and Sanofi Genzyme. E.E.L. has received research support from Biogen, LabCorp, Intus and Genentech. She has been a consultant for Bristol Myers Squibb, EMD Serono, Genentech, Sanofi Genzyme and NGM Bio.

Abstract

Multiple sclerosis (MS) is a complex genetically mediated autoimmune disease of the central nervous system where anti-CD20-mediated B cell depletion is remarkably effective in the treatment of early disease. While previous studies investigated the effect of B cell depletion on select immune cell subsets using flow cytometry-based methods, the therapeutic impact on patient immune landscape is unknown. In this study, we explored how B cell depleting therapies modulate the immune landscape using single-cell RNA sequencing (scRNAseq). We demonstrate that B cell depletion leads to cell type-specific changes in the abundance and function of cerebrospinal fluid (CSF) macrophages and peripheral blood monocytes. Specifically, a CSF-specific macrophage population with an anti-inflammatory transcriptomic signature and peripheral $CD16^+$ monocytes increased in frequency post-B cell depletion. This was accompanied by increases in TNFα messenger RNA and protein in monocytes post-B cell depletion, consistent with the finding that anti-TNFα treatment exacerbates autoimmune activity in MS. In parallel, B cell depletion induced changes in peripheral $CD4^+$ T cell populations, including increases in the frequency of $TIGIT^+$ regulatory T cells and marked decreases in the frequency of myelin peptide loaded-tetramer binding $CD4^+$ T cells. Collectively, this study provides an exhaustive transcriptomic map of immunological changes, revealing different cell-type specific reprogramming as a result of B cell depletion treatment in MS.

Introduction

While B cell depletion is efficacious in the treatment of various autoimmune diseases including rheumatoid arthritis and type 1 diabetes (1, 2), it has conferred remarkable therapeutic benefits in early relapsing remitting multiple sclerosis (MS) (3). The therapeutic benefits suggest a critical role of B cells in MS pathophysiology. While pathogenic myelin-reactive T cells (4, 5) with loss of regulatory T cell (Treg) function (6-8) have been established as mechanistic drivers of MS pathogenesis, accumulating evidence also directly implicates B cells as key contributors to loss of immune tolerance. The central role of B cells in MS pathophysiology is substantiated by the infiltration of B cells into MS lesions and CSF (9), the presence of ectopic meningeal B cell follicles adjacent to areas of focal cortical demyelination (10, 11), and the detection of oligoclonal IgG bands in the CSF as a diagnostic marker (12, 13).

Recent studies have investigated the effects of B cell depletion therapy with focus on neuronal cell types and T cells, as well as characterization of B cells before and after therapy (14-19). In this study, we unbiasedly explored how B cell depleting therapies modulate the immune landscape through the use of single-cell RNA sequencing (scRNAseq). B cell depletion in patients was accomplished through a humanized anti-CD20 antibody, ocrelizumab. We performed 5' scRNAseq on 18 paired peripheral blood mononuclear cells (PBMC) and five paired CSF samples obtained from incident MS patients pre- and post- B cell depletion treatment followed by flow cytometry validation of protein expression. The high dimensional single-cell data set allowed for simultaneous interrogation of the diverse immune populations in patient blood and CSF, and across disease states and treatment status.

Our data revealed increased frequency of a CSF macrophage population after B cell depletion that was paralleled by an increased frequency of $CD16^+$ monocytes in the periphery. We discovered that $CD16^+$ monocytes showed the highest upregulation of transcriptomic TNFα/NFκB signatures after ocrelizumab treatment compared to other cell types. The

transcriptional changes were confirmed with increases in TNFα protein expression in monocytes. Moreover, changes in the myeloid compartment were accompanied by increases in TIGIT expressing FoxP3^{+} Tregs and decreases in the frequency of circulating, myelin reactive CD4^{+} T cells. Our study provides an extensive transcriptomic map of immunological changes through the simultaneous interrogation of the diverse immune populations and their transcriptomic states before and after *in vivo* B cell depletion. This approach enabled us to discover distinct cell-type specific reprogramming associated with B cell depletion therapy in MS.

Results

$CD14^+CD68^+$ CSF cells increase in frequency post B cell depletion therapy

All patients were treatment naïve to any immunomodulatory therapy with new onset relapsing remitting MS (RRMS, Supplemental Table 1). To elucidate the effects of anti-CD20 treatment on the central nervous system (CNS) microenvironment, we analyzed 10 patient-matched fresh CSF samples from five RRMS patients pre- and post- B cell depletion treatment and performed an additional comparison with six fresh CSF samples from age-matched healthy donors. Post-treatment CSF samples were obtained at different time points: two at 6-month post-treatment, two at 12-month post-treatment, and one at 18-month post-treatment (Supplemental Table 1). After filtering of low-quality cells, scRNAseq yielded 60,704 total single cells from 16 CSF samples, including 15,122 cells from six healthy donor samples, 28,493 cells from five MS treatment-naïve samples and 17,089 cells from five MS post- treatment samples (Figure 1A).

After normalization and Harmony batch correction (see Methods), CSF cells were classified into 17 clusters (Figure 1B). To assess potential donor and sample variability, the frequencies of all immune populations in the CSF within each patient were profiled. Across all five patients, pre-treatment MS samples had lower proportions of the $CD14^+CD68^+$ myeloid-1 (Mac 1) cluster compared to healthy donors, and the frequencies of this cluster subsequently increased in all patients after B cell depletion treatment (Figure 1C, Supplemental Figure 1 and Supplemental Data 1). In parallel, from all five patients, 1536 B cells were found pre-treatment and only 188 B cells were detected post treatment, demonstrating effective B cell depletion of anti-CD20 antibodies. To further identify the immune subset most affected by B cell depletion therapy, we used Manifold Enhancement of Latent Dimensions (MELD) (20) to quantify the effect of B cell depletion treatment on all immune cell clusters in the CSF and discovered that the same Mac 1 cluster was the most enriched cell type after treatment (Figure 1D).

Dendritic cell (DC) clusters DC 1, DC 2, DC 3, and plasmacytoid DC (pDC) also showed enriched MELD score post-treatment. CSF scRNAseq data yielded 1423 cells in DC 1, 40 cells in DC 2, 35 cells in DC 3, and 256 cells in pDC from all patients across all timepoints. Due to low total cell numbers in DC 2 and DC 3 clusters, we focused dendritic cell analyses on DC 1 and pDC clusters. DC 1 cluster showed signatures of cDC2 with 440 healthy donor cells, 485 pre-treatment cells, and 498 post-treatment cells. pDC cluster had 37 healthy donor cells, 88 pre-treatment cells, and 131 post-treatment cells. Both DC 1 and pDC clusters did not show differences in MHC class I and class II expression before and after B cell depletion (Supplemental Figures 2A and 3A), and DC 1 did not show difference in expression for antigen presentation genes *CD74* and *CD86* pre- and post- treatment (Supplemental Figure 2B). We also profiled inflammatory genes in DC 1 and pDC clusters and observed that inflammatory genes were expressed in <5% of cells across all timepoints, with the exception of CD81 and CD86 being expressed in approximately 10-15% of pDC cells. Notably, CD40 expression was downregulated post-B cell depletion in both DC 1 and pDC, suggesting a potential decrease in DC activation and CD40-CD40L cellular interaction with B and T cells (Supplemental Figures 2C and 3B). In summary, B cell depletion did not appear to affect the expression of antigen presentation gens in DC 1 and pDC clusters, and DCs in the CSF expressed low transcript levels. Therefore, while the DC clusters exhibited similar trends of increased frequency post-treatment as the Mac 1 cluster, we prioritized downstream analyses on the Mac 1 subset as it had the highest MELD enrichment score and the least MELD score variability across patients.

$CD14^+CD68^+$ CSF cells are CSF- specific macrophages with microglia gene signatures

Previous studies reported $CD14^+$ CSF cells in various disease settings (21-23). We aimed to further evaluate the myeloid transcriptomic signatures in our patient CSF samples to define the $CD14^+CD68^+$ myeloid clusters. Mac 1 cluster exhibited high levels of myeloid (*TREM2, SPI1, CD68, MEF2C*) and monocyte (*CD14, FCGR3A, CSF1R, HLA-DRA*) transcriptomic signatures,

while lacking hallmark microglial genes such as *SALL1*, *P2RY12, FCRLS* and *TMEM119* (24, 25). In addition to pan-macrophage lineage markers *HLA-DR* and *CD14*, Mac 1 cluster also exhibited high expression of *APOE, CSF1R*, and genes that are expressed in extra parenchymal CSF macrophages such as *CST, TGFB1, MS4A7, LYZ, CLEC7A*. The mixture of microglial-like and monocytic genes and the abundant expression of *C1Q* and *HLA* class II genes classified this cluster as CSF-specific macrophages, distinct from monocytes, microglia and macrophages in other CNS tissues (Figure 1E) (26). Interestingly, memory CD4 cluster 5 exhibited a similar (albeit muted) signature, leading to the initial co-clustering of those two clusters despite coming from two separate lineages (Supplemental Figure 4A and B; see also Methods).

To further delineate the CSF macrophage subset, we computed pan-macrophage (*CD44, CCR2, CD45, CD206, CD163, CD274, CD169, MYB*), CNS macrophage (*TGFBI, MS4A7, MS4A6C, LYZ2, CD163, P2RX7, CST, CLEC7A*), and microglia (*P2Y12R, TMEM119, TREM2, CD115, CD172A, CD91, SPI1, FCRLS, SALL1, HEXB, SIGLECH, SLC2A5*) subset-specific gene module scores on all myeloid clusters in the CSF. The average expression of each of the transcriptomic programs were calculated then subtracted by the aggregated expression of randomly selected control genes using the AddModuleScore function from the Seurat package (27). The post-treatment enriched Mac 1 cluster scored the highest on the microglia module compared to other myeloid clusters. In contrast, $CD14^{+}CD68^{+}$ myeloid-2 (Mac 2) cluster scored higher on the pan-macrophage module compared to others (Figure 1F). Collectively, these transcriptomic signatures reflect the phenotypic diversity of the macrophage compartment in the CSF, and that anti-CD20 treatment increased the frequency of a specific subset of CSF macrophages within the CSF.

B cell depletion is associated with an anti-inflammatory phenotype in CSF macrophages

With the recent identification of CSF-specific macrophages (26) and the limited availability of patient CSF samples, the role of CSF macrophages in homeostasis and during MS pathogenesis

remains unclear. To better understand the treatment effect of B cell depletion on CSF macrophage immunophenotype, we performed differential gene expression (DE) analysis of pre- and post- treatment MS samples along with healthy donor CSF (Figure 2A, Supplemental Data 2). In the enriched Mac 1 cluster, hierarchical clustering on differentially expressed genes in MS pre-treatment vs. healthy donor cells revealed extensive changes, segregating cells from the two groups and highlighting alterations in MS patients (Supplemental Figure 5A). In contrast, hierarchical clustering between MS pre- and post- treatment CSF macrophages resulted in limited separation between the two groups (Supplemental Figure 5B). Among the genes upregulated after B cell depletion are oxidative phosphorylation genes (genes coding for NADH dehydrogenase and ATP synthase subunits) that are associated with anti-inflammatory macrophages (28, 29) (Figure 2A). In addition, genes involved in migration and endocytosis (*ITGB2, CSF1R, RAB11A, ANXA1*), as well as *HLA* class II genes, were downregulated after B cell depletion.

We observed increases in *HLA* class I and class II mRNA expression in Mac 1 cells from MS patient pre-treatment CSF as compared to healthy CSF Mac 1 cells. These increases in MHC expression from patients with MS decreased after B cell depletion (Figure 2B). We next applied the classical and alternative macrophage activation paradigm to delineate the neuroinflammatory state of CSF macrophages. Post-treatment Mac 1 cells exhibited transcriptomic downregulation in pro-inflammatory programming (*CCR7, JAK1, STAT1, IL1B, TNFA, TLR4, CD86*) and upregulation of anti-inflammatory genes (*IL-10, TGFB, CLEC7A*) In addition, we observed decrease of macrophage scavenger receptors (*CD163, MRC1, MSR1*) (Figure 2C). Taken together, the decreases in MHC class I and class II gene module scores suggest that B cell depletion reduces the probability of T cell activation through CSF macrophage antigen presentation. The increased expression of *IL10*, *TGFB*, and the oxidative phosphorylation pathway in CSF macrophages post-treatment suggests that B cell depletion therapy promotes the

resolution of inflammatory phenotype in CSF macrophages to restore homeostasis. Lastly, we computed transcriptomic signature scores based on peripheral monocytic gene modules and applied them to the CSF myeloid populations. We found that the enriched Mac 1 cluster scored the highest on the intermediate (*HLA-DR, CD14, CD11C, CD68, FCGR3A, CX3CR1, CSF1R, TLR4*) and nonclassical monocyte (*FCGR3A, CX3CR1, SLAN, CSF1R, CXCR1, CXCR4*) gene modules, whereas Mac 2 scored higher on the classical monocyte (*CD14, CCR2, CCR5, SELL, CD36, CD33, CD64*) gene module (Figure 2D). Thus, the transcriptomic resemblance of CSF macrophages to intermediate monocytes prompted us to investigate whether B cell depletion therapy modulates intermediate monocyte frequency in the periphery.

Increased abundance of CD16$^+$ monocytes post B cell depletion in MS patient PBMC

We next investigated whether alterations observed in the CSF post-B cell depletion were recapitulated in peripheral blood. We performed immune profiling with cryopreserved PBMC using scRNAseq from 18 newly diagnosed treatment-naïve patients with relapsing remitting RRMS whose samples were collected for both pre- and 6 months post-treatment (Supplemental Table 1 and Figure 3A). In our unsupervised analysis we retained 38 communities, which we assigned to coarse-grained immune cell types of interest (naïve T cells, memory CD4$^+$ T cells, cytotoxic lymphocytes, B cells, myeloid cells), and 18 fine-grained cell-types, as described in Figure 1B and Supplemental Figure 6, A and B. We classified communities into main lineages based on marker gene inspection and scoring cells against reference datasets using singleR software (Supplemental Figure 6C) (30).

Using MELD, we interrogated differences in abundance between the pre- and post-treatment samples. As expected, ocrelizumab treatment significantly decreased the abundance of B cells except for plasmablasts, which are known to downregulate CD20 that leads to loss of sensitivity to ocrelizumab-mediated depletion (Figure 3B). Given our CSF data, we next focused our attention on myeloid cells. We observed cellular enrichment in two myeloid clusters: CD16$^+$

monocytes and pDCs (Figure 3C). We confirmed these changes by formally testing for variations in frequency across all donors and observed that the increased frequency of $CD16^+$ monocytes was conserved across donors, while variations in pDC frequencies were more heterogenous (Figure 3D, Supplemental Figure 7A and Supplemental Data 3). This led us to focus solely on $CD16^+$ monocytes for further analyses. The $CD16^+$ monocytes cluster was the only cluster with detectable levels of *FCGR3A*, the gene encoding CD16 (Supplemental Figure 7B and D), and displayed markers associated with intermediate and non-classical monocytes. Scoring against the Monaco Immune reference with singleR revealed strong enrichment in intermediate and non-classical reference transcriptomes (Supplemental Figure 7C). To confirm this change, we measured circulating frequencies of various monocyte subpopulations using flow cytometry (Supplemental Figure 8A). There was a significant increase in $CD14^+CD16^+$ monocytes after B cell depletion treatment (Figure 3E).

Increased activation and TNFα production in $CD16^+$ monocytes post B cell depletion

We next determined whether $CD16^+$ monocytes harbor an altered transcriptomic state after B cell depletion. We computed differentially expressed genes while controlling for inter-individual variation using a generalized linear mixed model (glmm, as implemented in NEBULA (31) (Supplemental Data 4). We observed an increased expression of soluble molecules (*CCL5, CXCL8, TNFA*), surface receptors (*CD83, ITGB2, ITGA2B*), transcription factor *HIF1A*, and the NFκB signaling pathway (*TRAF1, NFKB2, REL, RELB, NFKBIA*) (Figure 4A). HIF1A has been shown to play an essential role in promoting anti-inflammatory activities in myeloid dendritic cells (32). In addition, CD83, a macrophage immune checkpoint marker, contributes to the resolution of inflammation and can induce Tregs in experimental models of MS (33, 34). $CD16^+$ monocytes showed downregulation in select transcription factors (*RXRA, IKZF1, KLF4, IRF4*) and CD81, a marker that facilitates monocytes homing to the CNS in EAE (35). Given the transcriptomic signature observed in $CD16^+$ monocytes, we validated changes at the protein level and observed

241 downregulation of CD81, and upregulation of monocyte activation marker *HLA-DR* using flow
242 cytometry (Figure 4B).

243 To further investigate the differentially expressed genes from the NFκB signaling pathway,
244 we next performed GSEA analysis in the enriched $CD16^+$ monocyte cluster using the Hallmark
245 gene sets collection. Consistent with the increased expression of NFκB-relevant transcription
246 factors, we observed enrichment in TNF-NFκB pathway (Figure 4C), as well as downregulation
247 related to JAK-STAT signaling gene sets (IL2, STAT5, IL6, JAK, STAT3, interferon alpha and
248 interferon gamma signaling pathways) post-treatment. Finally, to determine whether these
249 pathway modulations can also be observed in CSF macrophages (described in Figure 2), we
250 created custom gene sets based on PBMC DE and ran GSEA on the enriched Mac 1 CSF
251 macrophages to test for gene signature enrichment. We observed no significant enrichment of
252 PBMC gene sets in Mac 1 CSF macrophages (Supplemental Figure 9), suggesting the treatment-
253 mediated *in vivo* perturbation of biological pathways is tissue-specific and informed by the local
254 environment.

255 **B cell depletion induces ubiquitous response to TNFα in PBMC**

256 We next assessed whether the observed upregulation of TNF-NFκB pathway post-
257 treatment is cell-type specific. We computed differentially expressed genes for pre- vs post- B cell
258 depletion in all clusters (Supplemental Data 4), and used DE results to run GSEA analysis. We
259 observed TNF-NFκB pathway activation across most immune cell types post-ocrelizumab
260 treatment (Figure 5A). However, the downregulation of JAK-STAT related pathways was
261 restricted to $CD16^+$ monocytes, and the remaining or repopulating B cells post-treatment showed
262 increased expression of various gene sets related to cell survival (P53 Pathway, Apoptosis),
263 metabolism (Cholesterol Homeostasis) and JAK-STAT signaling (IL2-STAT5 and IL6-JAK-STAT3
264 pathways). Interestingly, clustering communities based on GSEA leading edge genes similarity
265 showed that the NFκB signaling enrichment was most similar between B cells and myeloid cells

while T lymphocytes formed a separate cluster, suggesting that transcriptomic responses to NFκB signaling differ between those lineages (Figure 5B).

Despite the ubiquitous TNF-NFκB pathway activation across cell types, $CD16^+$ monocytes showed the highest pre-treatment transcriptomic expression of TNFα and upregulated expression after treatment (Figure 5C). We also detected an increased post-treatment expression of TNFα in B cell cluster 3, MAIT, and DC clusters. To confirm changes in TNFα expression at the protein level, we enriched $CD14^+$ or $CD16^+$ monocytes from cryopreserved PBMCs and showed that LPS-stimulated monocytes from patients with MS expressed more TNFα post B cell depletion (Figure 5D). Increases of TNFα production by LPS-stimulated $CD14^+$ cells were similarly observed in MS patients treated with ocrelizumab by another group (36). However, there was no significant difference in TNFα in culture supernatant measured by ELISA (data not shown).

B cell depletion therapy reprograms the $CD4^+$ T helper cell compartment in both CSF and PBMC

Although $CD4^+$ T cells have been demonstrated as key pathogenic drivers of MS pathophysiology, limited changes were observed in the $CD4^+$ T cell compartment using singleR, MonacoImmune, and manual cellular annotation methods. Therefore, we applied a recently developed framework that captures a more granular classification and qualitative assessment of $CD4^+$ T cells based on scRNAseq data (Figure 6A) (37). This framework assigned $CD4^+$ T cells into five major clusters (cluster Layer 1 or L1) and 18 minor clusters (cluster Layer 2 or L2) by Symphony reference mapping (Figure 6B and Supplemental Figures 10A and 11A) and measured the activities of 12 pre-defined transcriptomic gene programs of $CD4^+$ T cells using non-negative matrix factorization projection (NMFproj).

At the major cluster L1 level, we did not detect any significant cell frequency changes in both CSF and PBMC (Supplemental Figures 10B and 11B). However, at the minor cluster L2 level,

290 there was a significant reduction of $CD4^+$ T effector memory (Tem) expressing T peripheral helper
291 (Tph) markers (Tem -Tph; *PDCD1*^{lo}*CXCR5*$^+$) in both CSF (padj= 1.88 x 10^{-2}) and PBMC (padj=
292 9.41x10^{-6}) tissues after B cell depletion treatment (Figure 6C and D, and Supplemental Figures
293 10C and 11C). In CSF alone, the frequency of $CD4^+$ T central memory (Tcm) expressing T
294 follicular helper (Tfh) markers (Tcm -Tfh; *PDCD1*$^+$*CXCR5*$^+$) was significantly reduced
295 (padj=9.36x10^{-3}) while the frequency of Tcm-Th0 was increased (padj=0.0472), suggesting a shift
296 toward a naïve phenotype post- B cell depletion in the CNS (Figure 6C and Supplemental Figures
297 10C). We also observed a significant increase of $CD4^+$ naïve T cells expressing *SOX4* (Tnaive
298 *SOX4*; *SOX4*$^+$*PECAM1*$^+$) (padj=4.29x10^{-3}) in the blood, a recent thymic emigrant population (38),
299 indicating that the peripheral blood $CD4^+$ T cell pool has been replenished by newly generated
300 $CD4^+$ T cells after treatment (Figure 6D and Supplemental Figure 11C).

301 We then assessed the changes in gene program activity quantified by NMFproj in each L2
302 subpopulation. We observed a significant reduction in cell types for NMF6 (Tfh-Feature or Tfh-F;
303 *MAF*, *CXCR5*) and NMF11 (Th1-F; *GZMK*, *EOMES*) post-treatment in both blood and CSF.
304 (Figure 6E and F, and Supplemental Data 5 and 6). Because NMF6 (Tfh-F) is predominantly high
305 in Tcm-Tfh, Tem-Tph, and intermediate Treg (Treg Int), the decrease of NMF6 (Tfh-F) in both
306 tissues indicates that B cell depletion treatment reduces their frequencies and potentially
307 represses the repopulation of these CD4 subtypes quantitatively and qualitatively. An increase of
308 NMF2 (Th17-F; *RORC*, *CCR6*) in the Tem population was observed in CSF, whereas NMF2
309 signature decreased in the blood (Figure 6E and F, and Supplemental Data 5 and 6). We also
310 observed increased NMF10 (Tissue-F; *JUNB*, *NFKBIA*) in blood after treatment (Figure 6F and
311 Supplemental Data 6). These observations suggested a redistribution of the $CD4^+$ T subsets
312 between the periphery and CNS. Altogether, these findings demonstrate that B cell depletion
313 notably alters the $CD4^+$ T cell compartment by reducing specific T cell populations such as Treg
314 Int, Tcm-Tfh, and Tem-Tph and modifying effector gene expression profiles such as repression

of NMF6 (Tfh-F) and NMF11 (Th1-F), which may be associated with its therapeutic efficacy in MS.

B cell depletion increases Tregs' frequency and suppressive phenotypes

Loss of Treg function has been repeatedly observed in patients with MS (8, 39). Our group showed MS susceptibility variant can modulate Treg function (40), and Treg function could be compromised during chronic inflammation (6, 41). We sub-clustered Tregs from scRNAseq PBMC data and compared L2 subpopulation frequencies to examine Treg alterations in more detail. We observed a significant decrease in naïve Tregs (*FOXP3, CCR7*, padj= 3.13×10^{-2}) and Treg Int (*FOXP3*, *FCRL3*, padj=6.79×10^{-3}) and an increase in effector Treg (Treg Eff) (*HLA-DR*s, *CD74*, padj=2.33×10^{-3}) in post-treatment samples. (Figure 7A and B). We also examined gene expression differences in the whole Treg population and found that *HLA-DR*s and *CD74*, which are the markers of Treg Eff, were increased. In contrast, *FCRL3*, a marker of Treg Int, was decreased after treatment (Figure 7C and Supplemental Figure 12A and B). These data suggest that B cell depletion skewed the Treg function toward the effector phenotype. Next, we examined the potential mediators of myeloid-Treg interactions using ligand-receptor prediction analysis (Figure 7D), Here, we observed a potential interaction between TNF receptor 2 (TNFR2, encoded by TNFRSF1B) on Tregs and TNF produced by myeloid cells.

Since TNFα is known to enhance the function of Tregs through TNFR2, which is preferentially expressed in Tregs (42, 43), we hypothesized that monocytes upregulated *TNFA* expression following B cell depletion and promoted Treg expansion through TNFR2 signaling. We measured Treg frequency using flow cytometry in 20 MS patient-matched PBMC samples pre- and post- ocrelizumab treatment. Within the 20 samples, 11 were from patients analyzed in our PBMC scRNAseq data, and 9 samples are from an additional cohort. We observed a significant increase in Treg frequency ($p < 0.001$) in post-treatment PBMC samples (Figure 7E). TIGIT protein is highly expressed in Treg Eff (44) (Supplemental Figure 12B and C) and has been shown

to associate with increases in functional activity in human and mice (45, 46). Therefore, we measured the frequency of TIGIT expressing Tregs after B cell depletion and observed a significant increase post- ocrelizumab treatment (Figure 7F). In summary, these data indicate that B cell depletion is associated with increased Treg frequency and effector function.

B cell depletion decreases myelin tetramer binding CD4$^+$ T cells

We and others have shown increases in the frequency of inflammatory myelin-reactive T cells recognizing a number of myelin antigens, presumably as a consequence of epitope spreading, in the circulation of MS patients. We have demonstrated the utility of using a panel of MHC class II (DRB1*15:01 or DRB1*04:01) tetramers loaded with myelin epitopes from myelin basic protein (MBP), proteolipid protein (PLP), and myelin oligodendrocyte glycoprotein (MOG) to study autoreactive T cells in the disease (4, 5, 47, 48). To increase the accuracy of detecting autoreactive T cells, we used both PE- and APC-conjugated tetramers with the same myelin composition (Supplemental Figure 8B) and MHC class II-associated invariant chain peptide (CLIP) tetramers as negative control (Supplemental Figure 8C). We initially examined a cohort of seven patients with HLA types of DRB1*15:01 and/or DRB1*04:01 pre- and post-B cell depletion and observed a marked decrease in the frequency of myelin PE- and APC-tetramer double positive (Tetramer DP) CD4$^+$ T cells (Figure 7G). In these data, decreased frequencies of CD45RA-CXCR5$^+$ cells and CCR6$^+$CXCR3$^-$ cells were observed in myelin tetramer binding CD4$^+$ T cells (Figure 7H). In a validation cohort of 9 MS patients, the frequency of myelin-specific T cells was significantly decreased after ocrelizumab treatment, and the frequencies of CD45RA$^-$CXCR5$^+$ cells and CCR6$^+$CXCR3$^-$ cells were also decreased in autoreactive CD4 T cells (Supplemental Figure 13A and B). Longitudinal kinetic analysis using fresh PBMC derived from a separate MS cohort (Supplemental Table 1) revealed significant decreases in the frequency of these autoreactive CCR6$^+$CXCR3$^+$ CD4$^+$ T cells at 6 months post-treatment, while no significant changes were observed in CCR6$^+$CXCR3$^+$ cells in non-tetramer reactive CD4$^+$ T cells. This trend

365 continued through 52 weeks (Supplemental Figure 13C). These results indicate that B cell
366 depletion might regulate the frequency of pathogenic myelin-reactive T cells.

Discussion

This study provides the first transcriptomic profiling dataset of MS patient blood and CSF pre- and post- B cell depletion therapy. Ocrelizumab, a humanized anti-CD20 monoclonal antibody, induces a systematic removal of naïve and memory B cells with ~98% efficacy in preventing new CNS lesions (3). Our unbiased analysis of the immune landscape using scRNAseq revealed that B cell depletion increased frequencies of CSF macrophages, and that these increased cell populations appeared to exhibit an anti-inflammatory phenotype. In the periphery, $CD16^+$ monocytes showed the highest level of TNFα messenger RNA expression pre-treatment, and B cell depletion further increased TNFα protein expression in these monocytes. Furthermore, after B cell depletion, we observed shifts in T cell populations, including decreased frequencies of Tem-Tph and Treg Int, along with Th1- and Tfh-type gene programs. Notably, we found that B cell depletion increased $TIGIT^+$ regulatory T cell frequency and decreased myelin tetramer-binding $CD4^+$ T cell frequency in the blood compartment.

The changes in myeloid cell frequency after B cell depletion were unexpected and revealed the power of an unbiased systems approach in dissecting the multitudes of immune-regulatory mechanisms of a highly efficacious therapy. We hypothesize that the dichotomous roles of myeloid cells in the pathogenesis of MS are due to the nature in which myeloid phenotype and function are orchestrated by the metabolic requirements in surrounding tissue environments. Soluble factors and cytokines shape macrophage differentiation and activate molecular programs that either exacerbate or attenuate disease (49). Systemic depletion of pathogenic B cells likely reduces the inflammatory states of multiple immune cell types in a feedback loop manner, and the subsequent recalibration of the cytokine milieu allows macrophages to differentiate in a steady-state environment and engage in disease-resolving transcription program to restore homeostasis. Given our study is limited to one post-treatment timepoint, it is possible that the changes we describe will normalize on the long term. Our ability to detect functional changes in

392 the CSF compartment were limited by the small sample size, variable post-treatment time-points,
393 and a small number of cells within the CSF macrophages clusters compared to other immune
394 populations. However, previous studies dissected changes in myeloid populations in the EAE
395 model and observed CNS-specific alterations of macrophages and microglia phenotypes during
396 the disease course (24, 25). Interestingly, Mrdjen et al. noted that border-associated
397 macrophages (BAMs) share similar profiles with pDC compared to other myeloid subsets. We
398 similarly observed that increased abundance of CSF macrophages was accompanied by
399 increased abundance of pDC (Figure 1). Finally, it should be noted that the increases in frequency
400 of CSF myeloid cells (Mac 1) are unlikely due to reduction in lymphocyte counts as the absolute
401 number of myeloid cells and lymphocytes are similarly decreased (data not shown).

402 With autoimmune exacerbations in patients with MS, peripheral blood monocytes receive
403 inflammatory cytokine signals and cross the blood- brain barrier with T cells leading to CNS
404 lesions (50, 51). While macrophages are the dominant cell type in these lesions, blood monocytes
405 also extravasate into the CSF and differentiate into CSF macrophages (52). However, it is critical
406 to not hyperactivate CSF macrophages in the process of phagocytosing waste to prevent
407 downstream immune activation of autoreactive lymphocytes (53). With B cell depletion, the
408 decrease in myeloid inflammatory cytokines enables CSF macrophages to receive pro-resolving
409 signals to execute their homeostatic function in mediating tissue repair (54). Our data suggest an
410 anti-inflammatory phenotype in CSF macrophage after B cell depletion treatment and that anti-
411 CD20 depletion therapy restores macrophage gene signatures similar to those of healthy controls.
412 Importantly, the inclusion of healthy donor CSF samples allows us to conclude that anti-CD20
413 treatment reprograms CSF macrophages toward a homeostatic or healthy state.

414 In the peripheral immune compartment, we uncovered a ubiquitous TNFα/NFκB activation
415 signature across a wide range of circulating immune cells post- B cell depletion. $CD14^{+}CD16^{+}$
416 monocytes have been shown to be a potent producer of TNFα (55), and our study suggests that

TNFα is a pleiotropic cytokine that potentially exerts anti-inflammatory effects after B cell depletion. B cell depletion confers moderate clinical effectiveness in treating rheumatoid arthritis whereas anti-TNFα clearly worsen MS immunopathogenesis (56). While the increased production of TNFα with a clinically effective treatment appears to be counter-intuitive, the beneficial role of TNFα in MS is substantiated by clinical trials showing anti-TNFα treatment in patients led to significant worsening of disease activity (57). Moreover, molecular dissection of MS risk allele rs1800693 located in the gene encoding the TNFR1 revealed the associated variant codes for a soluble form of TNFR1, which mimics TNFα blocking molecules (58, 59), again consistent with the observation that TNFα blockade leads to increased disease activity. In the context of chronic inflammation, this scenario where TNFα bears an anti-inflammatory role is reminiscent of the anti-tumor immune response. Specifically, in the tumor microenvironment, constant exposure to TNFα leads to immunosuppressive responses involving Tregs, B regulatory cells and myeloid-derived suppressor cells (60), and blocking TNFα leads to improved response to immune checkpoint blockade in an orthotopic melanoma mouse model (61). Additionally, identifying the precise signaling events leading to the observed transcriptomic changes is challenging given that the main TNFα signaling pathway is through NFκB, a highly ubiquitous signaling pathway. Thus, we cannot exclude other receptors signaling through NFκB are participating to the transcriptomic alterations observed post-treatment. Nevertheless, our rich dataset provides a non-biased road map for further mechanistic investigation in animal models.

Several of the established cell annotation methods that we employed were unable to detect changes in the CD4 T cell compartment. The biologically relevant signals could potentially be obfuscated due to the small frequency of myelin-specific T cells. Applying reference mapping with finer granular reference and gene program quantification by NMF, we were able to detect B cell depletion- mediated modulation of various T cell subsets. Although we did not focus on $CD8^+$ T cells, we and others previous showed that B-cell depletion leads to decrease in memory

442 $CD8^+CD20^+$ and central memory $CD8^+$ T cells (62, 63). Thus, we examined CD20 expression on
443 myelin tetramer-binding T cells. However, even in pre-B cell depletion samples, there were no
444 detectable CD20 positive cells in the tetramer positive T cell population. Additionally, the loss of
445 memory $CD8^+$ T cells correlated with a lower expression of CXCR3 CNS-related LFA-1 integrin
446 as well as a reduced antiviral cellular immune response (64). On the other hand, the frequency of
447 effector memory $CD4^+$ T cells decreased after ocrelizumab treatment, which is consistent with
448 previous result showing a decrease in $CD4^+$ effector memory T cells (65). In particular, we
449 demonstrate the ability of ocrelizumab to regulate activated autoreactive T cells by showing a
450 significant decrease in the frequency of $CD4^+$ $CCR6^+$ and $CD4^+$ $CXCR5^+$ T cells among cells
451 binding to myelin tetramer. While we were able to confirm the increase of effector Treg frequency
452 both by transcriptomic and protein expression, it will be of interest to more precisely identify
453 whether there are differences in myelin-specific and other antigens, as recent studies indicate
454 EBV infection of B cells is associated with the onset of MS (66).

455 Our T cell data suggests several mechanisms in which B cell depletion can lead to
456 modulation of T cell functionality. One potential model is that TNFα from myeloid cells engages
457 TNFR2 on Tregs leading to suppression of autoreactive T cells after B cell depletion in RRMS
458 patients. It is established that for Treg-mediated immunosuppression, the induction of an
459 appropriate effector phenotype is essential (67, 68). In this study, we revealed that ocrelizumab
460 treatment induced the formation of an Treg effector phenotype at both RNA and protein levels
461 and increased the number of Treg cells. Hence, the enhancement of Treg function following B
462 cell depletion may be contributing to the therapeutic effect. Alternatively, as first shown by
463 Lanzavecchia et al. (69), B cells may be the key antigen presenting cell and their depletion may
464 result in loss of autoreactive effector or memory T cells. Similarly, the decrease of MHC
465 expression on myeloid cells may also support this hypothesis. In summary, our systems analysis
466 identified a series of immunoregulatory pathways associated with B cell depletion. This is perhaps

not surprising as the genetic architecture of MS and other autoimmune diseases suggests that multiple pathways are involved in disease pathogenesis (70). It is possible that different immunosuppressive pathways become activated among patients, leading to marked decreases of autoreactive myelin reactive T cells in the blood compartment. Clinically, it will be relevant to connect those immune parameters to potential changes in long term disease progression.

Our analyses comparing immune cells in CSF and blood also highlight distinct changes across compartments, suggesting that regulation of CNS homing mechanisms could be affected by anti-CD20 therapies. Considering the potential disease-mediating and homeostatic functions in the myeloid compartment, future analyses can be designed with a myeloid cell focus using fresh tissue for higher sensitivity in protein detection. Nevertheless, these datasets are exploratory and provide a critical starting point that will require well-designed *in vitro* and *ex vivo* assays and appropriate animal models to fully elucidate the perturbational effects of B cell depletion on the functionality of the immune system.

Material and Methods

Sex as a biological variable

Our study examined male and female participants, and similar findings are reported for both sexes.

Patient Cohorts

All patients had early onset relapsing remitting MS and had not been on previous immunomodulatory treatments. A small subset of patients had received IV solumedrol within 3 months of blood draw. Eighteen patients undergoing single cell RNA seq studies had CSF analysis prior to the initiation of treatment, and five of those subjects had repeat lumbar punctures, as outlined in the results section. A total of six age-matched healthy controls had lumbar punctures, and those results were previously reported (50). Patient pre-treatment CSF samples were obtained for clinical diagnosis, patient post-treatment and healthy donor CSF samples were obtained under voluntary enrollment into our research study in accordance to IRB regulations. Samples were collected at disease onset and prior to scheduled B cell depletion infusions (on the same day), with the exception of 3 patients: samples from patients MS1189, MS1092 and MS1056 were collected 1-, 28- and 59-days post-infusion, respectively. An additional four subjects had flow cytometric analysis only. Patient characteristics are summarized in Supplemental Table 1.

Sample preparation for scRNAseq

Fresh patient CSF samples were centrifuged, and cells were immediately processed using 10x Genomics 5Pv1 chemistry. Samples were collected prior to infusion of B cell depletion therapy. In the CSF sample cohort, four of the patients were administered ocrelizumab B cell depletion treatment, and one was treated with rituximab. Patient PBMCs were isolated from whole blood using Lymphoprep (STEMCELL) density gradient centrifugation. All patients were administered

ocrelizumab B cell depletion in the PBMC cohort. Cryopreserved patient-matched pre-treatment and 6-month post-treatment PBMCs were thawed and processed within the same experimental batch using 10x Genomics 5Pv1 chemistry. For PBMCs, TCR libraries were generated along with the gene expression libraries.

scRNAseq QC

PBMC and CSF libraries were sequenced at 20,000 read pairs per cell on Illumina NovaSeq instrument. Fastq files were processed using cellranger version 3.1.0 mapping to GRCh38 human reference genome. Alignment and quantitation were performed with the "cellranger count" command for each emulsion (using the 2020-A 10x genomics human reference), to generate unique molecular identifier (UMI) count matrices.

For CSF, Data QC was performed in R using the Seurat package. Low quality cells were filtered out based on mitochondria percent, UMI counts and number of features for individual samples. Samples were then merged, log10-transformed, and batch corrected using Harmony.

For PBMCs, we first filtered extreme outliers by excluding droplets with less than 1500 UMI counts, or less than 850 unique genes detected. As distribution of those parameters varied across emulsions, we median-centered the log10-transformed number of unique genes detected and removed low quality droplets with less than 1,100 unique genes detected or more than 2.5% mapping of UMI counts mapping to mitochondrial genes. We also removed potential doublets by filtering out droplets with more than 2,600 unique genes detected.

scRNAseq analysis

Dimensionality reduction and clustering

For cells passing quality control, we normalized UMI counts by dividing each count by the total number of counts per cell. We then multiplied normalized counts by 10,000 and added a pseudo count of 1 before log-transformation. We computed the stabilized variance of each gene using the variance-stabilizing transformation (VST) and retained genes with stabilized variance >

1 for principal component analysis (PCA). Genes mapping to the T cell receptor (TCR), the B cell receptor (BCR) and the Y chromosome were excluded from PCA analysis. We computed the first 50 principal components (PCs) using a partial singular value decomposition method, based on the implicitly restarted Lanczos bidiagonalization algorithm (IRLBA), as implemented in the *Seurat* R package (71). To correct for systematic differences across samples, we applied harmony integration (72) to the first 50 PC loadings and retained 30 harmony-corrected PCs to build nearest neighbor graphs for visualization using Uniform Manifold Approximation and Projection (UMAP) (minimum distance = 0.5, spread = 10), and community detection using Louvain algorithm, as implemented in *Seurat*. We also computed a relative likelihood of cells being observed in specific experimental conditions using Manifold Enhancement of Latent Dimensions (MELD) (20). We quantified the effects of sample-level variables (i.e. pre- vs post-treatment) across the transcriptomic space, using harmony-corrected PC loadings as input. MELD employs graph signal processing to model the cellular state space as a network, connecting cells with similar transcriptomic profiles. It generates an Enhanced Experimental Signal (EES) to estimate the likelihood of observing cells from each condition at every point in the manifold. This continuous measure facilitates the derivation of cell subsets that are affected by the sample-level conditions.

We embedded cells into 2 UMAP dimensions and applied Louvain algorithm. We annotated cluster cell types based on individual gene expression and the SingleR automatic annotation package using the MonacoImmuneData PBMC reference (73). We tested for variation in clusters frequency in the CSF and in the blood separately by modelling the per-sample cluster frequencies using a beta distribution in a generalized linear model framework, as implemented in the *betareg* R package, using the logit link function (74). We also used an alternative constrained beta binomial model based on counts, implemented in the sccomp R package (75), which yielded similar results (See Supplemental Data 1 and 3).

Differential gene expression (DE)

For DE testing at the single cell level in CSF, we used a fix-effect negative binomial model as implemented in the DESeq2 package (76), supplemented with a recent optimization for single cell RNAseq data (77). We excluded low expression genes based on a UMI count per cell < 0.005, as well as ribosomal, mitochondrial, TCR, BCR. We evaluated differences in counts with treatment or disease status predictor, adding categorical donor information as covariates. We then computed shrunk log fold changes using adaptative shrinkage methods implemented in the *ashr* R package (78) (using a mixture of normal distributions). P values were computed by fitting a reduced model and using a likelihood ratio test, and multiple comparison correction was performed by FDR (Benjamini & Hochberg method) across all genes tested, as implemented in the DESeq2 package. Genes with FDR < 0.1 were considered differentially expressed. For differential expression testing at the single cell level in PBMCs, we used a negative binomial mixed linear model as implemented in the NEBULA package (31). We then used shrunken log fold changes as a ranking metrics to run geneset enrichment analysis (GSEA).

Treg volcano and ligand-receptor analyses

Volcano plot displaying differential expression analysis performed using *nebula* comparing pre- and post-treatment Treg population. Among genes with differential expression (BH < 0.05) and average expression >0.1, those that encode surface proteins (based on Cell Surface Protein Atlas surfaceome protein database) were selectively labeled (79). NicheNet (*nichenetr)* (80) was used to identify predicted ligand-receptor interactions between myeloid populations and Tregs, will a particular focus on potential ligands that are differentially regulated in myeloid cells with B cell depletion treatment. Tregs were selected as the “receiver cell type”, including all expressed genes as potential receptors. Myeloid cells were selected as the “sender cell type”, limiting the set of potential ligands to the combined list of genes differentially expressed with B cell depletion treatment in myeloid cell clusters (see *NEBULA* analysis). Predicted ligand-receptor interactions

were displayed as a heat map in which ligands (expressed by myeloid cells) were plotted against receptors (expressed by Tregs) and weighted by prior interaction potential.

CD4⁺ T cell automatic labeling and quantification of gene programs

The PBMC and CSF data were processed using the pipeline developed in the previous study (37) to assign CD4⁺ T cell clusters. This pipeline employs Azimuth (44) for the extraction of CD4⁺ T cells and uses Symphony (81) for predicting CD4⁺ T cell clusters. For interpretability, 'Treg Act' has been renamed to 'Treg Int' from the original literature. We tested for variation in cluster frequency by modeling the per-sample cluster frequencies using a beta distribution in a generalized linear model framework, as implemented in the *betareg* R package. For the assessment of TIGIT protein expression, we used CITE-seq data from PBMCs deposited in GSE164378 and performed reference mapping using the pipeline. Additionally, a 12-dimensional qualitative evaluation was conducted on the extracted CD4⁺ T cells using NMFproj (82). We applied a generalized linear model to assess feature changes per cluster (37).

Flow cytometry analysis

Frozen PBMCs were used for flow cytometry validation, except longitudinal myelin tetramer staining were performed on fresh PBMCs (n=4). Patient peripheral blood mononuclear cells were stained with a ViaKrome 808 Fixable Viability dye following the manufacturer's instructions. Cells were then labeled with surface antibodies for 30 min at 4°C. For intracellular staining, cells were fixed and permeabilized with BD Cytofix/Cytoperm Buffer (BD Biosciences) for 10 min at room temperature, then washed with phosphate-buffered saline. Intracellular proteins were stained in permeabilization buffer (eBioscience) for 30 min at 4 °C. Antibody details are provided in Supplemental Table 2. For TNFα staining, monocytes were enriched from cryopreserved PBMCs using EasySep™ Human Monocyte Enrichment Kit without CD16 Depletion Kit (STEMCELL technologies). Enriched monocytes were stimulated with 100ng/ml LPS for 4h at 37 °C before

staining. To investigate myelin tetramer reactive T cells, APC- or PE- conjugated tetramers which were composed by DRB1*15:01 (loaded with MBP, MOG and PLP) or DRB1*04:01 (loaded with MOG and PLP) were used (4, 48). Myelin tetramers were incubated with cells for 30 min at 37°C before staining with antibodies. Cells were acquired on a BD Symphony flow cytometer with FACSDiva (BD Pharmingen) and data were analyzed with FlowJo software v.10 (Treestar). Changes in frequencies were tested using the *betareg* model, as described in the *scRNAseq analysis* section. Changes in mean fluorescence intensities (MFI) were tested using a generalized linear model with gaussian distribution and a log link function.

Peptide loading

Biotinylated monomers were diluted to a concentration of 0.5 mg/mL with 0.1 M phosphate buffer and incubated with 0.4 mg/ml of at 37°C for 72 h in the presence of 2.5 mg/ml n-Octyl β-D-glucopyranoside (OG) and 1 mM Pefabloc SC (Sigma–Aldrich, St. Louis, MO). Peptide loaded monomers were subsequently conjugated into tetramers using R-PE streptavidin (ThermoFisher Scientific, Waltham, MA) or fluorochromes of interest at a molar ratio of 8:1. Myelin peptide sequences are listed in the Supplemental Table 3.

Statistics

All statistical analyses were performed using the R programming language using generalized linear models. Where appropriate, we included a donor covariate to model the paired nature of samples (before and after treatment). P values were computed using Wald test of regression coefficients.

Study Approval

This study was approved by the Institutional Review Board at Yale University. CSF and blood samples were obtained from healthy donors and MS patients with informed consent.

Data and code availability statement:

All raw scRNAseq data generated in this study are deposited on dbGAP (phs003938.v1.p1). This newly generated data was analyzed jointly with published scRNAseq of CSF samples from 6 healthy controls and 4 MS patients at diagnostic (MS1102, MS1131, MS1171, MS1228) already deposited on dbGAP (phs002222.v1.p1). All code used for genomics analysis is available on github (https://github.com/ImmuneAxisa/Ocrevus_manuscript) and figshare (https://doi.org/10.6084/m9.figshare.28204532), along with intermediate analysis files. Supporting data values are available in supplementary data.

Author contributions:

JW, JM, IY, TSS, PPA and DAH designed experiments. JM, LZ, KR, NBP, IY and JP conducted experiments. JW, JM, YY, MED, NS, EEL collected and analyzed data. CWC, AH, RP, CR advised on data analyses. TSS, PPA and DAH supervised data analyses. JW, JM, TSS, PPA and DAH wrote the manuscript, integrating feedback from all co-authors.

Acknowledgement:

The authors thank Rahul Dhodapkar for helpful discussions on computational data analysis. Chuan He for technical support and Kathryn Miller-Jensen for experimental input and discussion. This work was supported by NIH grants (P01 AI073748, U19 AI089992 U24 AI11867, R01 AI22220, UM 1HG009390, P01 AI039671, P50 CA121974, R01 CA227473) and Race to Erase MS to D.A.H. and National MS Society to D.A.H. and grants from Genentech and F. Hoffmann-La Roche Ltd as part of Integrative Neuroscience Collaborations Network.

References

1. Lee DSW, Rojas OL, and Gommerman JL. B cell depletion therapies in autoimmune disease: advances and mechanistic insights. *Nat Rev Drug Discov.* 2021;20(3):179-99.
2. Pescovitz MD, Greenbaum CJ, Krause-Steinrauf H, Becker DJ, Gitelman SE, Goland R, et al. Rituximab, B-lymphocyte depletion, and preservation of beta-cell function. *N Engl J Med.* 2009;361(22):2143-52.
3. Hauser SL, Bar-Or A, Comi G, Giovannoni G, Hartung HP, Hemmer B, et al. Ocrelizumab versus Interferon Beta-1a in Relapsing Multiple Sclerosis. *N Engl J Med.* 2017;376(3):221-34.
4. Cao Y, Goods BA, Raddassi K, Nepom GT, Kwok WW, Love JC, et al. Functional inflammatory profiles distinguish myelin-reactive T cells from patients with multiple sclerosis. *Sci Transl Med.* 2015;7(287):287ra74.
5. Ota K, Matsui M, Milford EL, Mackin GA, Weiner HL, and Hafler DA. T-cell recognition of an immunodominant myelin basic protein epitope in multiple sclerosis. *Nature.* 1990;346(6280):183-7.
6. Dominguez-Villar M, Baecher-Allan CM, and Hafler DA. Identification of T helper type 1-like, Foxp3+ regulatory T cells in human autoimmune disease. *Nat Med.* 2011;17(6):673-5.
7. Sumida T, Lincoln MR, Ukeje CM, Rodriguez DM, Akazawa H, Noda T, et al. Activated beta-catenin in Foxp3(+) regulatory T cells links inflammatory environments to autoimmunity. *Nat Immunol.* 2018;19(12):1391-402.
8. Viglietta V, Baecher-Allan C, Weiner HL, and Hafler DA. Loss of functional suppression by CD4+CD25+ regulatory T cells in patients with multiple sclerosis. *J Exp Med.* 2004;199(7):971-9.
9. Jain RW, and Yong VW. B cells in central nervous system disease: diversity, locations and pathophysiology. *Nat Rev Immunol.* 2022;22(8):513-24.
10. Lucchinetti CF, Popescu BF, Bunyan RF, Moll NM, Roemer SF, Lassmann H, et al. Inflammatory cortical demyelination in early multiple sclerosis. *N Engl J Med.* 2011;365(23):2188-97.
11. Magliozzi R, Howell O, Vora A, Serafini B, Nicholas R, Puopolo M, et al. Meningeal B-cell follicles in secondary progressive multiple sclerosis associate with early onset of disease and severe cortical pathology. *Brain.* 2007;130(Pt 4):1089-104.
12. Comi G, Bar-Or A, Lassmann H, Uccelli A, Hartung HP, Montalban X, et al. Role of B Cells in Multiple Sclerosis and Related Disorders. *Ann Neurol.* 2021;89(1):13-23.
13. Reich DS, Lucchinetti CF, and Calabresi PA. Multiple Sclerosis. *N Engl J Med.* 2018;378(2):169-80.
14. Hecker M, Fitzner B, Boxberger N, Putscher E, Engelmann R, Bergmann W, et al. Transcriptome alterations in peripheral blood B cells of patients with multiple sclerosis receiving immune reconstitution therapy. *J Neuroinflammation.* 2023;20(1):181.
15. Nissimov N, Hajiyeva Z, Torke S, Grondey K, Bruck W, Hausser-Kinzel S, et al. B cells reappear less mature and more activated after their anti-CD20-mediated depletion in multiple sclerosis. *Proc Natl Acad Sci U S A.* 2020;117(41):25690-9.

16. Quendt C, Ochs J, Hausser-Kinzel S, Hausler D, and Weber MS. Proinflammatory CD20(+) T Cells are Differentially Affected by Multiple Sclerosis Therapeutics. *Ann Neurol.* 2021;90(5):834-9.
17. Sabatino JJ, Jr., Wilson MR, Calabresi PA, Hauser SL, Schneck JP, and Zamvil SS. Anti-CD20 therapy depletes activated myelin-specific CD8(+) T cells in multiple sclerosis. *Proc Natl Acad Sci U S A.* 2019;116(51):25800-7.
18. Ulutekin C, Galli E, Schreiner B, Khademi M, Callegari I, Piehl F, et al. B cell depletion attenuates CD27 signaling of T helper cells in multiple sclerosis. *Cell Rep Med.* 2024;5(1):101351.
19. Wang AA, Luessi F, Neziraj T, Possnecker E, Zuo M, Engel S, et al. B cell depletion with anti-CD20 promotes neuroprotection in a BAFF-dependent manner in mice and humans. *Sci Transl Med.* 2024;16(737):eadi0295.
20. Burkhardt DB, Stanley JS, 3rd, Tong A, Perdigoto AL, Gigante SA, Herold KC, et al. Quantifying the effect of experimental perturbations at single-cell resolution. *Nat Biotechnol.* 2021;39(5):619-29.
21. Esaulova E, Cantoni C, Shchukina I, Zaitsev K, Bucelli RC, Wu GF, et al. Single-cell RNA-seq analysis of human CSF microglia and myeloid cells in neuroinflammation. *Neurol Neuroimmunol Neuroinflamm.* 2020;7(4).
22. Farhadian SF, Mehta SS, Zografou C, Robertson K, Price RW, Pappalardo J, et al. Single-cell RNA sequencing reveals microglia-like cells in cerebrospinal fluid during virologically suppressed HIV. *JCI Insight.* 2018;3(18).
23. Ramesh A, Schubert RD, Greenfield AL, Dandekar R, Loudermilk R, Sabatino JJ, Jr., et al. A pathogenic and clonally expanded B cell transcriptome in active multiple sclerosis. *Proc Natl Acad Sci U S A.* 2020;117(37):22932-43.
24. Jordao MJC, Sankowski R, Brendecke SM, Sagar, Locatelli G, Tai YH, et al. Single-cell profiling identifies myeloid cell subsets with distinct fates during neuroinflammation. *Science.* 2019;363(6425).
25. Mrdjen D, Pavlovic A, Hartmann FJ, Schreiner B, Utz SG, Leung BP, et al. High-Dimensional Single-Cell Mapping of Central Nervous System Immune Cells Reveals Distinct Myeloid Subsets in Health, Aging, and Disease. *Immunity.* 2018;48(2):380-95 e6.
26. Munro DAD, Movahedi K, and Priller J. Macrophage compartmentalization in the brain and cerebrospinal fluid system. *Sci Immunol.* 2022;7(69):eabk0391.
27. Stuart T, Butler A, Hoffman P, Hafemeister C, Papalexi E, Mauck WM, 3rd, et al. Comprehensive Integration of Single-Cell Data. *Cell.* 2019;177(7):1888-902 e21.
28. Ip WKE, Hoshi N, Shouval DS, Snapper S, and Medzhitov R. Anti-inflammatory effect of IL-10 mediated by metabolic reprogramming of macrophages. *Science.* 2017;356(6337):513-9.
29. Wculek SK, Heras-Murillo I, Mastrangelo A, Mananes D, Galan M, Miguel V, et al. Oxidative phosphorylation selectively orchestrates tissue macrophage homeostasis. *Immunity.* 2023;56(3):516-30 e9.
30. Aran D, Looney AP, Liu L, Wu E, Fong V, Hsu A, et al. Reference-based analysis of lung single-cell sequencing reveals a transitional profibrotic macrophage. *Nat Immunol.* 2019;20(2):163-72.

31. He L, Davila-Velderrain J, Sumida TS, Hafler DA, Kellis M, and Kulminski AM. NEBULA is a fast negative binomial mixed model for differential or co-expression analysis of large-scale multi-subject single-cell data. *Commun Biol.* 2021;4(1):629.
32. Sanmarco LM, Rone JM, Polonio CM, Fernandez Lahore G, Giovannoni F, Ferrara K, et al. Lactate limits CNS autoimmunity by stabilizing HIF-1alpha in dendritic cells. *Nature.* 2023;620(7975):881-9.
33. Grosche L, Knippertz I, Konig C, Royzman D, Wild AB, Zinser E, et al. The CD83 Molecule - An Important Immune Checkpoint. *Front Immunol.* 2020;11:721.
34. Peckert-Maier K, Langguth P, Strack A, Stich L, Muhl-Zurbes P, Kuhnt C, et al. CD83 expressed by macrophages is an important immune checkpoint molecule for the resolution of inflammation. *Front Immunol.* 2023;14:1085742.
35. Dijkstra S, Kooij G, Verbeek R, van der Pol SM, Amor S, Geisert EE, Jr., et al. Targeting the tetraspanin CD81 blocks monocyte transmigration and ameliorates EAE. *Neurobiol Dis.* 2008;31(3):413-21.
36. Geladaris A, Hausser-Kinzel S, Pretzsch R, Nissimov N, Lehmann-Horn K, Hausler D, et al. IL-10-providing B cells govern pro-inflammatory activity of macrophages and microglia in CNS autoimmunity. *Acta Neuropathol.* 2023;145(4):461-77.
37. Yasumizu Y, Takeuchi D, Morimoto R, Takeshima Y, Okuno T, Kinoshita M, et al. Single-cell transcriptome landscape of circulating CD4(+) T cell populations in autoimmune diseases. *Cell Genom.* 2024;4(2):100473.
38. Kimmig S, Przybylski GK, Schmidt CA, Laurisch K, Mowes B, Radbruch A, et al. Two subsets of naive T helper cells with distinct T cell receptor excision circle content in human adult peripheral blood. *J Exp Med.* 2002;195(6):789-94.
39. Dominguez-Villar M, and Hafler DA. Regulatory T cells in autoimmune disease. *Nat Immunol.* 2018;19(7):665-73.
40. Axisa PP, Yoshida TM, Lucca LE, Kasler HG, Lincoln MR, Pham GH, et al. A multiple sclerosis-protective coding variant reveals an essential role for HDAC7 in regulatory T cells. *Sci Transl Med.* 2022;14(675):eabl3651.
41. Baeten P, Van Zeebroeck L, Kleinewietfeld M, Hellings N, and Broux B. Improving the Efficacy of Regulatory T Cell Therapy. *Clin Rev Allergy Immunol.* 2022;62(2):363-81.
42. Chen X, Wu X, Zhou Q, Howard OM, Netea MG, and Oppenheim JJ. TNFR2 is critical for the stabilization of the CD4+Foxp3+ regulatory T. cell phenotype in the inflammatory environment. *J Immunol.* 2013;190(3):1076-84.
43. Torrey H, Kuhtreiber WM, Okubo Y, Tran L, Case K, Zheng H, et al. A novel TNFR2 agonist antibody expands highly potent regulatory T cells. *Sci Signal.* 2020;13(661).
44. Hao Y, Hao S, Andersen-Nissen E, Mauck WM, 3rd, Zheng S, Butler A, et al. Integrated analysis of multimodal single-cell data. *Cell.* 2021;184(13):3573-87 e29.
45. Joller N, Lozano E, Burkett PR, Patel B, Xiao S, Zhu C, et al. Treg cells expressing the coinhibitory molecule TIGIT selectively inhibit proinflammatory Th1 and Th17 cell responses. *Immunity.* 2014;40(4):569-81.
46. Lucca LE, Axisa PP, Singer ER, Nolan NM, Dominguez-Villar M, and Hafler DA. TIGIT signaling restores suppressor function of Th1 Tregs. *JCI Insight.* 2019;4(3).

47. Markovic-Plese S, Fukaura H, Zhang J, al-Sabbagh A, Southwood S, Sette A, et al. T cell recognition of immunodominant and cryptic proteolipid protein epitopes in humans. *J Immunol.* 1995;155(2):982-92.
48. Raddassi K, Kent SC, Yang J, Bourcier K, Bradshaw EM, Seyfert-Margolis V, et al. Increased frequencies of myelin oligodendrocyte glycoprotein/MHC class II-binding CD4 cells in patients with multiple sclerosis. *J Immunol.* 2011;187(2):1039-46.
49. Park MD, Silvin A, Ginhoux F, and Merad M. Macrophages in health and disease. *Cell.* 2022;185(23):4259-79.
50. Pappalardo JL, Zhang L, Pecsok MK, Perlman K, Zografou C, Raddassi K, et al. Transcriptomic and clonal characterization of T cells in the human central nervous system. *Sci Immunol.* 2020;5(51).
51. Goverman J. Autoimmune T cell responses in the central nervous system. *Nat Rev Immunol.* 2009;9(6):393-407.
52. Herz J, Filiano AJ, Wiltbank AT, Yogev N, and Kipnis J. Myeloid Cells in the Central Nervous System. *Immunity.* 2017;46(6):943-56.
53. Monney L, Sabatos CA, Gaglia JL, Ryu A, Waldner H, Chernova T, et al. Th1-specific cell surface protein Tim-3 regulates macrophage activation and severity of an autoimmune disease. *Nature.* 2002;415(6871):536-41.
54. Li R, Rezk A, Miyazaki Y, Hilgenberg E, Touil H, Shen P, et al. Proinflammatory GM-CSF-producing B cells in multiple sclerosis and B cell depletion therapy. *Sci Transl Med.* 2015;7(310):310ra166.
55. Belge KU, Dayyani F, Horelt A, Siedlar M, Frankenberger M, Frankenberger B, et al. The proinflammatory CD14+CD16+DR++ monocytes are a major source of TNF. *J Immunol.* 2002;168(7):3536-42.
56. Li P, Zheng Y, and Chen X. Drugs for Autoimmune Inflammatory Diseases: From Small Molecule Compounds to Anti-TNF Biologics. *Front Pharmacol.* 2017;8:460.
57. Kunchok A, Aksamit AJ, Jr., Davis JM, 3rd, Kantarci OH, Keegan BM, Pittock SJ, et al. Association Between Tumor Necrosis Factor Inhibitor Exposure and Inflammatory Central Nervous System Events. *JAMA Neurol.* 2020;77(8):937-46.
58. Gregory AP, Dendrou CA, Attfield KE, Haghikia A, Xifara DK, Butter F, et al. TNF receptor 1 genetic risk mirrors outcome of anti-TNF therapy in multiple sclerosis. *Nature.* 2012;488(7412):508-11.
59. Harroud A, and Hafler DA. Common genetic factors among autoimmune diseases. *Science.* 2023;380(6644):485-90.
60. Montfort A, Colacios C, Levade T, Andrieu-Abadie N, Meyer N, and Segui B. The TNF Paradox in Cancer Progression and Immunotherapy. *Front Immunol.* 2019;10:1818.
61. Bertrand F, Montfort A, Marcheteau E, Imbert C, Gilhodes J, Filleron T, et al. TNFalpha blockade overcomes resistance to anti-PD-1 in experimental melanoma. *Nat Commun.* 2017;8(1):2256.
62. van Puijfelik F, Blok KM, Klein Kranenbarg RAM, Rip J, de Beukelaar J, Wierenga-Wolf AF, et al. Ocrelizumab associates with reduced cerebrospinal fluid B and CD20(dim) CD4(+) T cells in primary progressive multiple sclerosis. *Brain Commun.* 2024;6(1):fcae021.

63. Shinoda K, Li R, Rezk A, Mexhitaj I, Patterson KR, Kakara M, et al. Differential effects of anti-CD20 therapy on CD4 and CD8 T cells and implication of CD20-expressing CD8 T cells in MS disease activity. *Proc Natl Acad Sci U S A.* 2023;120(3):e2207291120.
64. Mathias A, Pantazou V, Perriot S, Canales M, Jones S, Oberholster L, et al. Ocrelizumab Impairs the Phenotype and Function of Memory CD8(+) T Cells: A 1-Year Longitudinal Study in Patients With Multiple Sclerosis. *Neurol Neuroimmunol Neuroinflamm.* 2023;10(2).
65. Garcia A, Dugast E, Shah S, Morille J, Lebrun-Frenay C, Thouvenot E, et al. Immune Profiling Reveals the T-Cell Effect of Ocrelizumab in Early Relapsing-Remitting Multiple Sclerosis. *Neurol Neuroimmunol Neuroinflamm.* 2023;10(3).
66. Bjornevik K, Cortese M, Healy BC, Kuhle J, Mina MJ, Leng Y, et al. Longitudinal analysis reveals high prevalence of Epstein-Barr virus associated with multiple sclerosis. *Science.* 2022;375(6578):296-301.
67. Sakaguchi S, Mikami N, Wing JB, Tanaka A, Ichiyama K, and Ohkura N. Regulatory T Cells and Human Disease. *Annu Rev Immunol.* 2020;38:541-66.
68. Sumida TS, Cheru NT, and Hafler DA. The regulation and differentiation of regulatory T cells and their dysfunction in autoimmune diseases. *Nat Rev Immunol.* 2024;24(7):503-17.
69. Lanzavecchia A. Antigen-specific interaction between T and B cells. *Nature.* 1985;314(6011):537-9.
70. Pisetsky DS. Pathogenesis of autoimmune disease. *Nat Rev Nephrol.* 2023;19(8):509-24.
71. Butler A, Hoffman P, Smibert P, Papalexi E, and Satija R. Integrating single-cell transcriptomic data across different conditions, technologies, and species. *Nat Biotechnol.* 2018;36(5):411-20.
72. Korsunsky I, Millard N, Fan J, Slowikowski K, Zhang F, Wei K, et al. Fast, sensitive and accurate integration of single-cell data with Harmony. *Nat Methods.* 2019;16(12):1289-96.
73. Monaco G, Lee B, Xu W, Mustafah S, Hwang YY, Carre C, et al. RNA-Seq Signatures Normalized by mRNA Abundance Allow Absolute Deconvolution of Human Immune Cell Types. *Cell Rep.* 2019;26(6):1627-40 e7.
74. Cribari-Neto F, and Zeileis A. Beta Regression in R. *J Stat Softw.* 2010;34(2):1-24.
75. Mangiola S, Roth-Schulze AJ, Trussart M, Zozaya-Valdes E, Ma M, Gao Z, et al. sccomp: Robust differential composition and variability analysis for single-cell data. *Proc Natl Acad Sci U S A.* 2023;120(33):e2203828120.
76. Love MI, Huber W, and Anders S. Moderated estimation of fold change and dispersion for RNA-seq data with DESeq2. *Genome Biol.* 2014;15(12):550.
77. Ahlmann-Eltze C, and Huber W. glmGamPoi: fitting Gamma-Poisson generalized linear models on single cell count data. *Bioinformatics.* 2021;36(24):5701-2.
78. Stephens M. False discovery rates: a new deal. *Biostatistics.* 2017;18(2):275-94.
79. Bausch-Fluck D, Hofmann A, Bock T, Frei AP, Cerciello F, Jacobs A, et al. A mass spectrometric-derived cell surface protein atlas. *PLoS One.* 2015;10(3):e0121314.
80. Browaeys R, Saelens W, and Saeys Y. NicheNet: modeling intercellular communication by linking ligands to target genes. *Nat Methods.* 2020;17(2):159-62.

81. Kang JB, Nathan A, Weinand K, Zhang F, Millard N, Rumker L, et al. Efficient and precise single-cell reference atlas mapping with Symphony. *Nat Commun.* 2021;12(1):5890.
82. Yasumizu Y, Ohkura N, Murata H, Kinoshita M, Funaki S, Nojima S, et al. Myasthenia gravis-specific aberrant neuromuscular gene expression by medullary thymic epithelial cells in thymoma. *Nat Commun.* 2022;13(1):4230.

885 **Figures and legends**

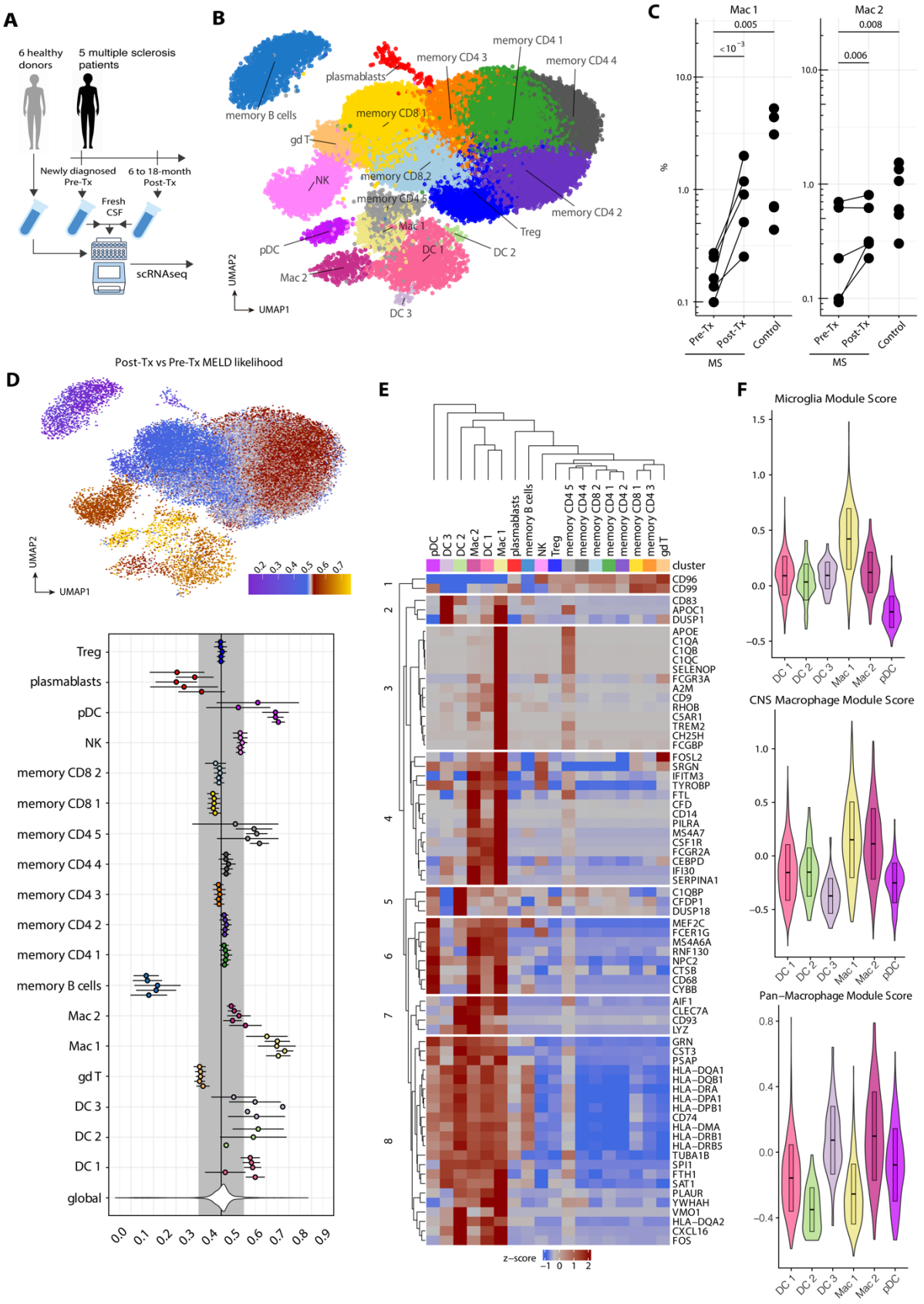
A
6 healthy donors
5 multiple sclerosis patients
Newly diagnosed Pre-Tx
6 to 18-month Post-Tx
Fresh CSF
scRNAseq
B
memory B cells
plasmablasts
memory CD4 1
memory CD4 3
memory CD4 4
memory CD8 1
gd T
NK
memory CD8 2
memory CD4 5
memory CD4 2
Mac 1
Treg
pDC
DC 1
DC 2
Mac 2
DC 3
UMAP2
UMAP1
C
Mac 1
Mac 2
0.005
<10−3
0.008
0.006
%
Pre-Tx
Post-Tx
Control
MS
D
Post-Tx vs Pre-Tx MELD likelihood
UMAP2
UMAP1
Treg
plasmablasts
pDC
NK
memory CD8 2
memory CD8 1
memory CD4 5
memory CD4 4
memory CD4 3
memory CD4 2
memory CD4 1
memory B cells
Mac 2
Mac 1
gd T
DC 3
DC 2
DC 1
global
E
cluster
z-score
F
Microglia Module Score
CNS Macrophage Module Score
Pan−Macrophage Module Score
DC 1
DC 2
DC 3
Mac 1
Mac 2
pDC

Figure 1. Microglia-like CSF macrophages increase in frequency in MS patients post- B cell depletion therapy. **(A)** Healthy donor and MS patient sample collection scheme for scRNAseq analysis (n = 6 healthy donors, n= 5 MS patients pre-treatment, n= 5 matched MS patients post-treatment). **(B)** UMAP dimensionality reduction plot of immune cell clusters detected in CSF of healthy donor and MS patients (n= 60,704 single cells, 17 immune cell clusters). **(C)** CSF macrophage cluster frequency pre- and post- B cell depletion therapy across all five MS patients. **(D)** MELD likelihood enrichment UMAP and patient level summary values (mean+/- SEM, n= 5 MS patients) post- B cell depletion therapy of all immune clusters in the ©. **(E)** Heatmap of myeloid-related genes, showing average expression across all immune cell types. **(F)** All myeloid clusters in the CSF scored against microglia, CNS macrophage, and pan- macrophage gene modules. (P values were computed using Wald test of regression coefficients).

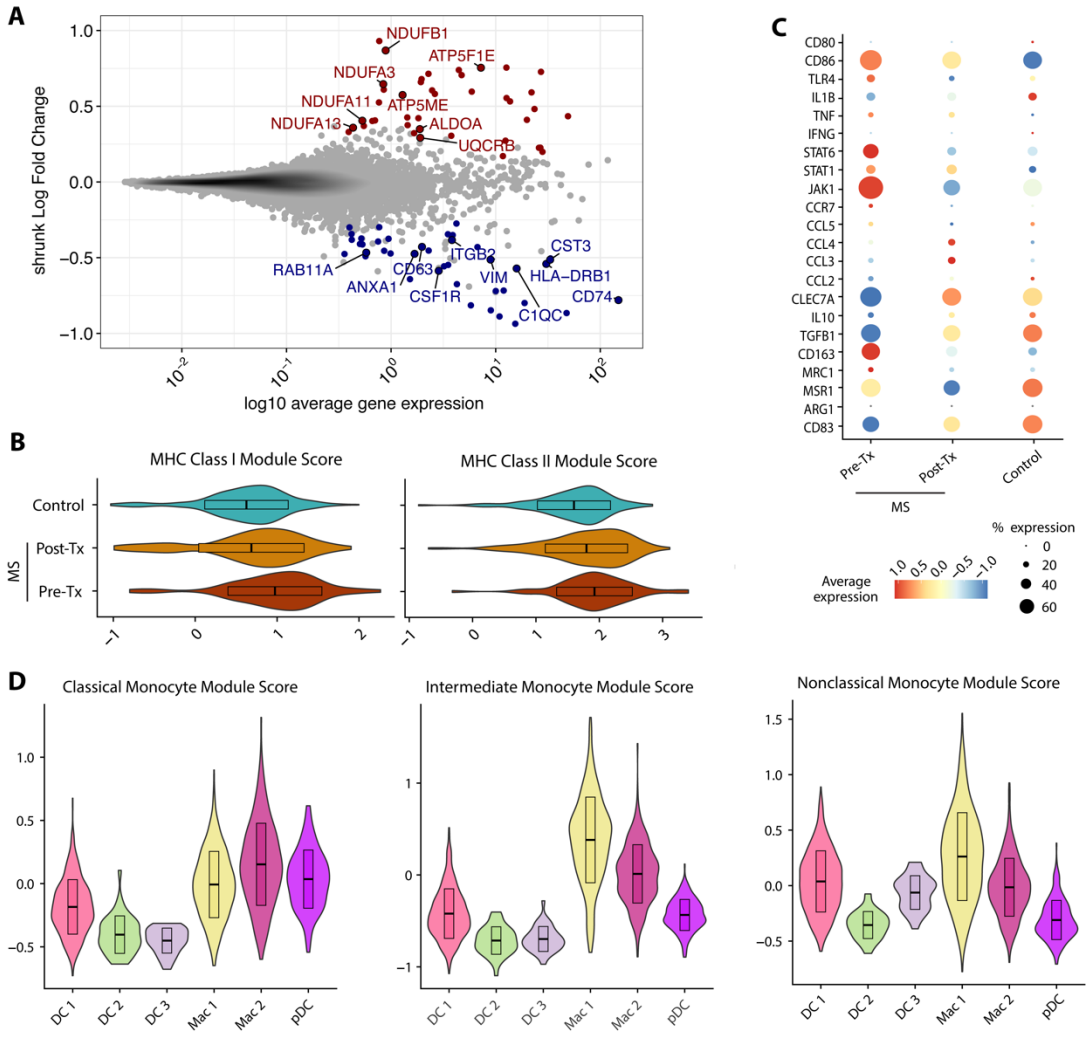
A
shrunk Log Fold Change
log10 average gene expression
NDUFB1
ATP5F1E
NDUFA3
NDUFA11
ATP5ME
NDUFA13
ALDOA
UQCRB
CST3
ITGB2
RAB11A
CD63
VIM
HLA-DRB1
ANXA1
CSF1R
CD74
C1QC
B
MHC Class I Module Score
MHC Class II Module Score
Control
Post-Tx
Pre-Tx
MS
C
CD80
CD86
TLR4
IL1B
TNF
IFNG
STAT6
STAT1
JAK1
CCR7
CCL5
CCL4
CCL3
CCL2
CLEC7A
IL10
TGFB1
CD163
MRC1
MSR1
ARG1
CD83
Pre-Tx
Post-Tx
Control
MS
% expression
Average expression
D
Classical Monocyte Module Score
Intermediate Monocyte Module Score
Nonclassical Monocyte Module Score
DC 1
DC 2
DC 3
Mac 1
Mac 2
pDC

899

Figure 2. Enriched CSF macrophages present anti-inflammatory phenotype in MS patients post- B cell depletion therapy. Gene expression analyses of CSF macrophages were performed by comparing cells from healthy donors (n=6) and pre- and post- B cell depletion therapy MS patient samples (n=5). **(A)** Mean abundance plot depicting differentially expressed genes (FDR <0.1) in the Mac 1 cluster from MS patients pre- and post- B cell depletion. Blue: downregulated post-treatment, red: upregulated post-treatment. **(B)** MHC class I and class II gene module scores of healthy donor, MS pre-treatment, and MS post-treatment Mac 1 cells. **(C)** Dot plot depicting myeloid inflammatory and anti-inflammatory gene expression in healthy donors and MS patients pre- and post-treatment. **(D)** Gene module scores of all CSF myeloid clusters against peripheral monocyte gene signatures. Top: classical monocyte module score, middle: intermediate monocyte module score, bottom: nonclassical monocyte module score.

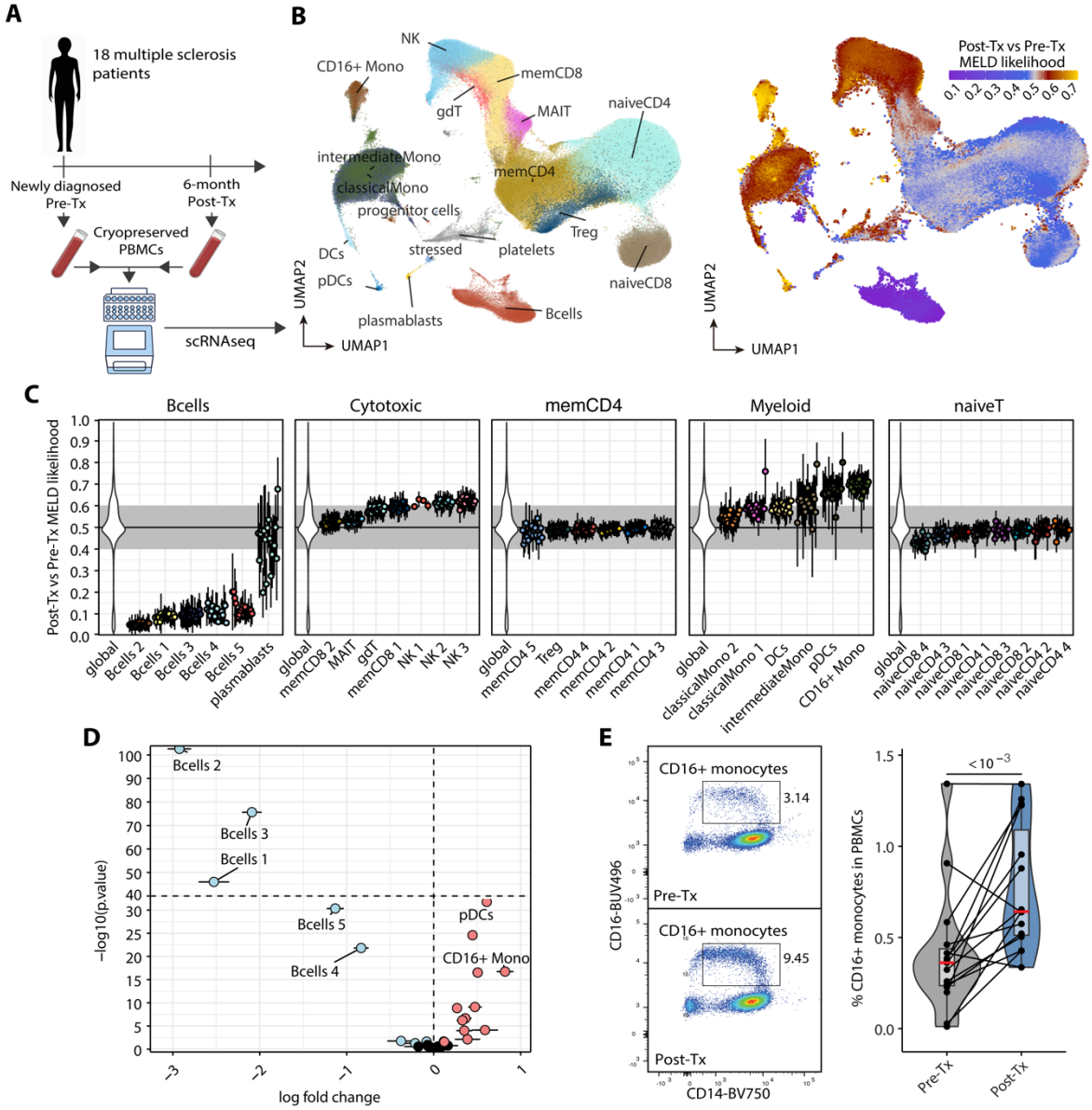
A
18 multiple sclerosis patients
Newly diagnosed Pre-Tx
6-month Post-Tx
Cryopreserved PBMCs
scRNAseq
B
NK
CD16+ Mono
memCD8
gdT
MAIT
naiveCD4
intermediateMono
classicalMono
memCD4
progenitor cells
Treg
DCs
stressed
platelets
pDCs
naiveCD8
plasmablasts
Bcells
UMAP1
UMAP2
Post-Tx vs Pre-Tx MELD likelihood
0.1 0.2 0.3 0.4 0.5 0.6 0.7
C
Bcells
Cytotoxic
memCD4
Myeloid
naiveT
Post-Tx vs Pre-Tx MELD likelihood
global Bcells 2 Bcells 1 Bcells 3 Bcells 4 Bcells 5 plasmablasts
global memCD8 2 MAIT gdT memCD8 1 NK 1 NK 2 NK 3
global memCD4 5 Treg memCD4 4 memCD4 2 memCD4 1 memCD4 3
global classicalMono 2 classicalMono 1 DCs intermediateMono pDCs CD16+ Mono
global naiveCD8 4 naiveCD4 3 naiveCD8 1 naiveCD4 1 naiveCD8 3 naiveCD8 2 naiveCD4 2 naiveCD4 4
D
Bcells 2
Bcells 3
Bcells 1
Bcells 5
Bcells 4
pDCs
CD16+ Mono
−log10(p.value)
log fold change
E
CD16+ monocytes
3.14
Pre-Tx
CD16+ monocytes
9.45
Post-Tx
CD16-BUV496
CD14-BV750
< 10 −3
% CD16+ monocytes in PBMCs
Pre-Tx
Post-Tx

911

Figure 3. Increased CD16^{+} monocytes abundance after anti-CD20 treatment. (A) experimental design of pre- and post-treatment (anti-CD20) PBMC samples from MS patients (n=18) for droplet-based scRNAseq using 10x genomics platform. **(B)** UMAP of annotated cell types (left) and overlayed MELD likelihoods for post-treatment status (right). **(C)** MELD likelihood patient level summary values (mean+/- SEM) per fine-grained clusters and main cell types. **(D)** fine-grained community frequency changes post-treatment (log fold change mean estimate +/-SE from beta regression, see methods). (**E)** Flow cytometry validation of CD16^{+} monocyte frequency changes in MS patients PBMCs. (P values were computed using Wald test of regression coefficients).

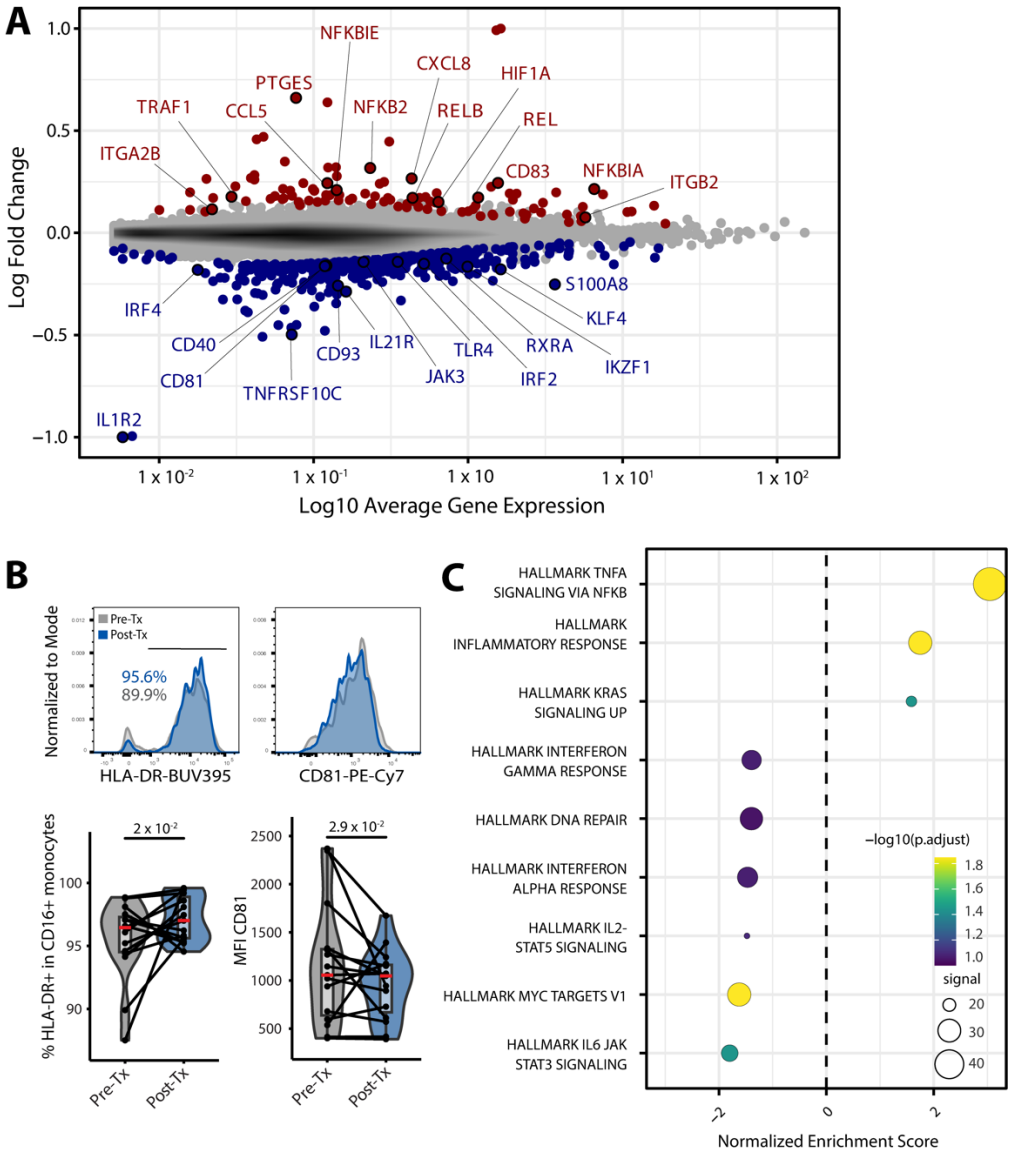

Figure 4. Differential gene expression in CD16⁺ monocyte post-treatment. (**A)** Mean abundance (MA) plot of gene expression changes, differentially expressed genes (DGE) are highlighted in red (upregulated post-treatment), or blue (downregulated post-treatment). (**B)** Flow cytometry of HLA-DR and CD81 expression in CD16⁺ monocytes (n=16). (**C)** GeneSet Enrichment Analysis (GSEA) using the Hallmark genesets in CD16⁺ monocytes. (**D)** Custom GSEA analysis of PBMC monocytes post-treatment signature genesets (up- and downregulated genes) tested on CSF macrophage Mac 1 dataset (From Figure 1). (P values were computed using Wald test of regression coefficients).

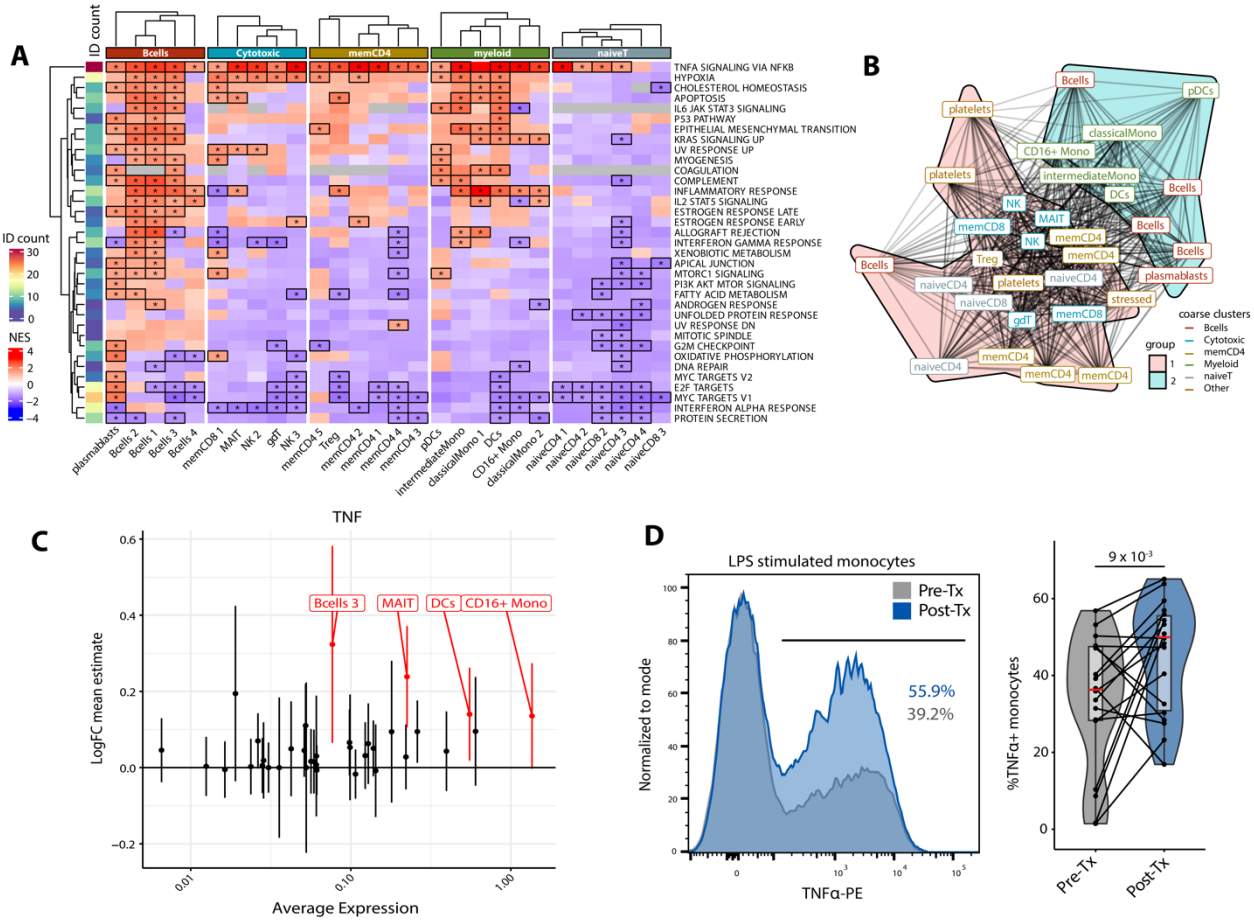

Figure 5. Geneset enrichment analysis (GSEA) of anti-CD20 gene expression alterations across cell types. (A) Heatmap of normalized enrichment scores (NES) from post-treatment GSEA analyses run for each cluster shows ubiquitous increase in TNFα-NFκB pathway. Differentially enriched genesets are highlighted with a *. "ID count" depicts the number of times a geneset is found enriched across communities. **(B)** Overlap graph-analysis of leading-edge genes for the "TNFα signaling via NFκB" geneset across cell types highlights two sets of signatures: B and myeloid cells vs. T cells. **(C)** Pre- and post- treatment fold change of *TNFA* transcript across clusters (differential expression is highlighted in red). **(D)** *In vitro* validation of TNFα upregulation pre- and post- B cell depletion at the protein level in MS patient monocytes (n= 18) by intracellular flow cytometry staining after LPS stimulation. (P values were computed using Wald test of regression coefficients).

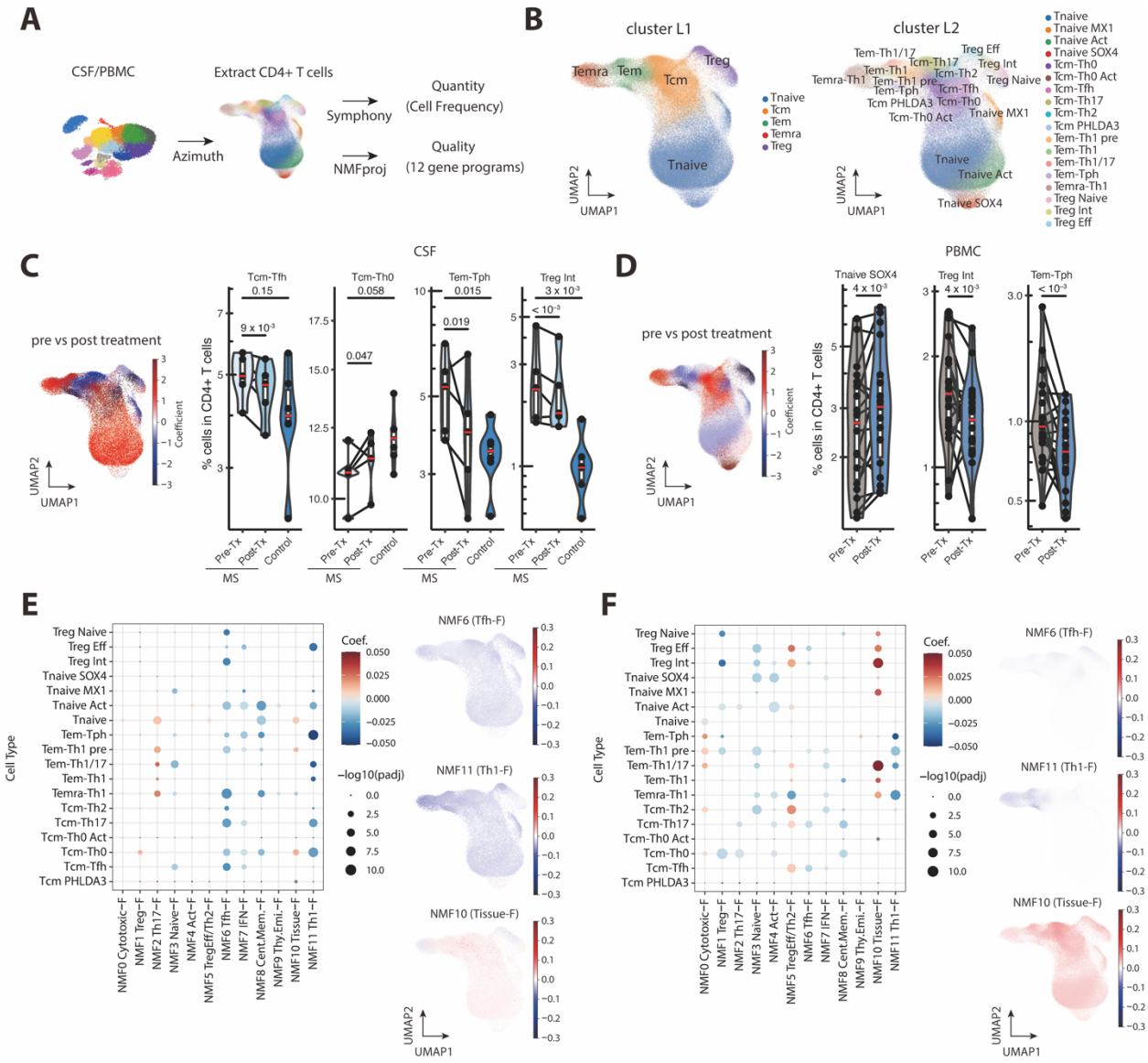

Figure 6. Detailed Analysis of CD4$^+$ T Cell Alterations Following Anti-CD20 Treatment. (A) Schematic illustration of the analysis of CD4$^+$ T cells using a reference mapping and NMFproj. From CSF and PBMC samples, CD4$^+$ T cells were extracted using Azimuth, and detailed CD4$^+$ T clusters were predicted using Symphony. The 12 gene programs were calculated using NMFproj. **(B)** Inferred CD4$^+$ T cell clusters on UMAP plot. The clusters were assigned to either a major cluster (L1) or a detailed cluster (L2) level. **(C and D)** Cell frequency changes after anti-CD20 treatment in CSF (C) and PBMC (D). Coefficients of cell frequency change per cluster L2 quantified GLM are visualized on the UMAP plot (left). The populations with cell frequency

increases post-B cell depletion treatment are shown in red. $CD4^+$ T cluster frequency pre- and post-B cell depletion therapy (right). Substantially altered clusters are shown. See Supplemental Figures 10C and 11C for additional details. **(E and F)** Alterations of gene programs extracted by NMFproj after anti-CD20 treatment in CSF (E) and PBMC (F). Dot plots depicting NMF cell feature changes in each cell type (left). Dot colors show coefficients, and sizes show the significance of GLM (method). The coefficient of gene program change per cluster for some gene programs was shown on UMAP plots (right). Annotations and representative genes of gene programs are following; NMF0 (Cytotoxic-Feature or Cytotoxic-F; *GZMB*, *CX3CR1*), NMF1 (Treg-F; *FOXP3*, *IL2RA*), NMF2 (Th17-F; *RORC*, *CCR6*), NMF3 (Naive-F; *CCR7*, *BACH2*), NMF4 (Activation-F or Act-F; *DACT1*, *CDK6*), NMF5 (TregEff/Th2-F; *HLA-DR*s, *CCR10*), NMF6 (Tfh-F; *MAF*, *CXCR5*), NMF7 (Interferon-F or IFN-F; *OAS1*, *MX1*), NMF8 (Central Memory-F; *CRIP2*, *PLP2*), NMF9 (Thymic Emigrant-F; *SOX4*, *PECAM1*), NMF10 (Tissue-F; *JUNB*, *NFKBIA*) NMF11 (Th1-F; *GZMK*, *EOMES*). (P values were computed using Wald test of regression coefficients).

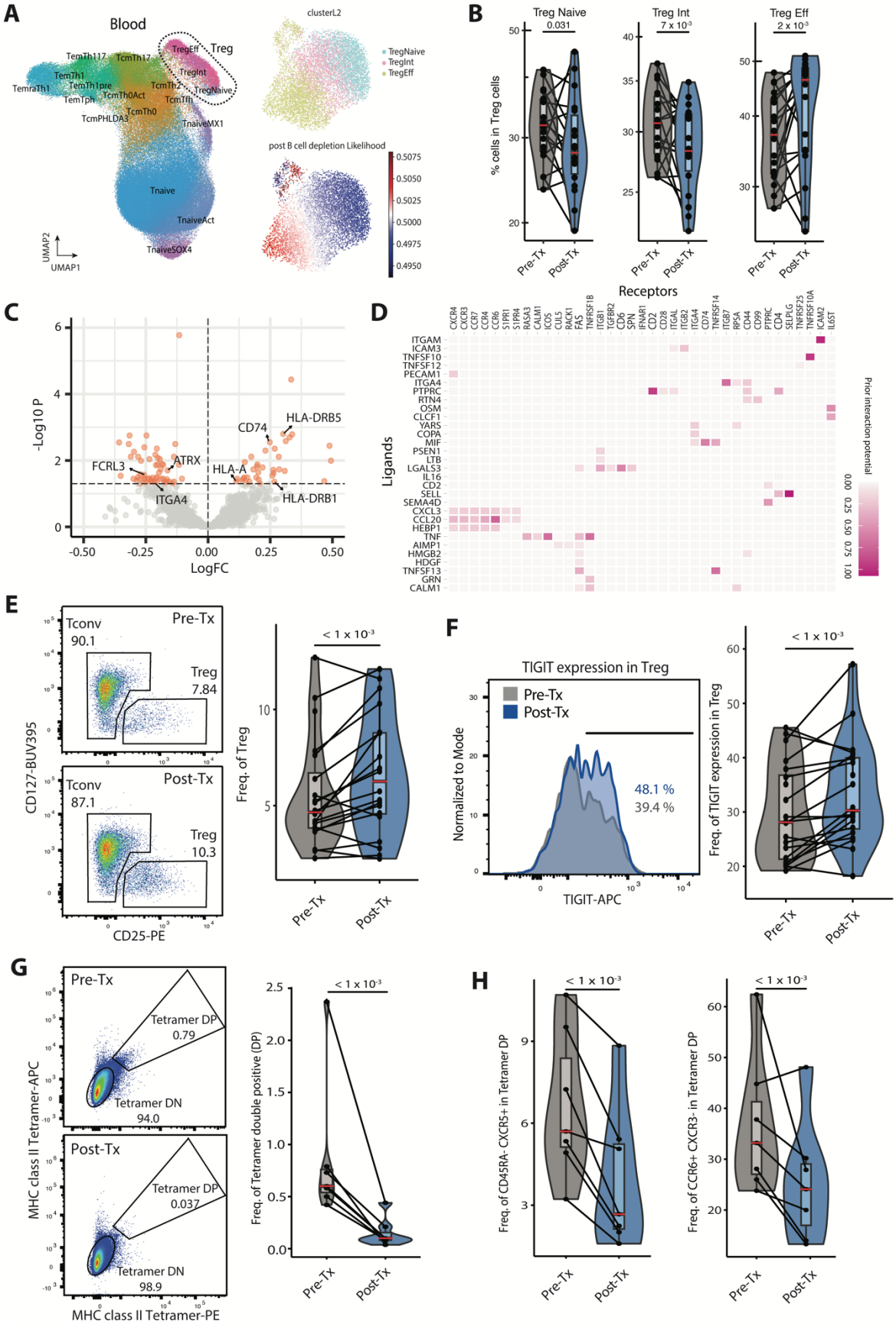
A
Blood
Treg
TemTh117
TcmTh17
TregEff
TregInt
TemTh1
TemTh1pre
TemraTh1
TcmTh2
TregNaive
TemTph
TcmTh0Act
TcmTfh
TcmTh0
TcmPHLDA3
TnaiveMX1
Tnaive
TnaiveAct
TnaiveSOX4
UMAP2
UMAP1
clusterL2
TregNaive
TregInt
TregEff
post B cell depletion Likelihood
0.5075
0.5050
0.5025
0.5000
0.4975
0.4950
B
Treg Naive
0.031
Treg Int
7 x 10-3
Treg Eff
2 x 10-3
% cells in Treg cells
Pre-Tx
Post-Tx
C
-Log10 P
LogFC
CD74
HLA-DRB5
FCRL3
ATRX
HLA-A
ITGA4
HLA-DRB1
D
Receptors
Ligands
Prior interaction potential
E
Tconv
90.1
Pre-Tx
Treg
7.84
Tconv
87.1
Post-Tx
Treg
10.3
CD127-BUV395
CD25-PE
< 1 x 10-3
Freq. of Treg
F
TIGIT expression in Treg
Pre-Tx
Post-Tx
Normalized to Mode
48.1 %
39.4 %
TIGIT-APC
< 1 x 10-3
Freq. of TIGIT expression in Treg
G
Pre-Tx
Tetramer DP
0.79
Tetramer DN
94.0
Post-Tx
Tetramer DP
0.037
Tetramer DN
98.9
MHC class II Tetramer-APC
MHC class II Tetramer-PE
< 1 x 10-3
Freq. of Tetramer double positive (DP)
H
< 1 x 10-3
Freq. of CD45RA- CXCR5+ in Tetramer DP
< 1 x 10-3
Freq. of CCR6+ CXCR3- in Tetramer DP

965

Figure 7. B cell depletion induces an increase in TIGIT$^+$ Tregs and reduces autoreactive T cells. (A) Visualization of Treg population extraction and changes after B cell depletion treatment. Predicted CD4$^+$ T clusters and Tregs (dotted line) on UMAP plot (left). Re-embedding of extracted Tregs using UMAP (top right). B cell depletion treatment associated relative likelihood in Treg populations calculated using MELD (bottom right). **(B)** Frequency changes of each subpopulation within the Treg group. **(C)** Volcano plot depicting differentially expressed genes in Tregs, particularly highlighting genes encoding surface proteins. **(D)** Heatmap displaying predicted interactions between myeloid cell-derived ligands (limited to genes differentially regulated with B cell depletion treatment) and Treg-derived receptors, weighted by prior interaction potential. **(E and F)** Flow cytometry data of Tregs frequency (E) and TIGIT protein expression of Tregs (F) in MS patient PBMC (n=20) after B cell depletion treatment, **(G)** Flow cytometry analysis of myelin tetramer-reactive CD4$^+$ T cell frequency at pre-treatment and 6-month post-treatment timepoints (n=7). **(H)** Tfh (CD45RA$^-$ CXCR5$^+$) cells in tetramer-reactive CD4$^+$ T cells and Th17 (CCR6$^+$CXCR3$^-$) cells in tetramer-reactive CD4$^+$ T cells frequencies at pre-treatment and 6-month post-treatment timepoints (n=7). (P values were computed using Wald test of regression coefficients).